Journal of Structural Geology 177 (2023) 104981

Contents lists available at ScienceDirect

Journal of Structural Geology

journal homepage: www.elsevier.com/locate/jsg

# Along- and across-strike variation of damage zone parameters in the Kornos-Aghios Ioannis normal fault, Lemnos Island, Greece

L.R. Berio [a,*], F. Balsamo [a], M. Pizzati [a], F. Storti [a], M. Curzi [b], G. Viola [c]

[a] Università di Parma, Dipartimento di Scienze Chimiche, della Vita e della Sostenibilità Ambientale, NEXT - Natural and Experimental Tectonics Research Group, Parco Area delle Scienze 157/A, 43124, Parma, Italy
[b] Dipartimento di Scienze della Terra, Sapienza Università di Roma, Piazzale Aldo Moro 5, 00185, Roma, Italy
[c] Università degli Studi di Bologna, Dipartimento di Scienze Biologiche, Geologiche e Ambientali, Via Zamboni 67, 40126, Bologna, Italy

ARTICLE INFO

*Keywords:*
Fault architecture
Damage zone
Fracture topology
Silicified fault

ABSTRACT

The Kornos-Aghios Ioannis Fault (KAIF) is an extensional fault system that deformed Lower Miocene volcanic rocks and Middle Eocene to Lower Miocene turbidite sandstones at shallow depth (<1 km). The fault system is exposed for about 10 km and consists of two major NW-SE-striking segments connected by an E-W-striking one. This structural architecture provides the opportunity to study the variation of damage zone parameters (i.e., damage zone width, fracture density, attitude of deformation structures, and fracture connectivity) in wall, tip and intersecting damage zones. The >122 m wide tip damage zone has a width greater than the wall and intersecting damage zones (72.6 and 50.9m, respectively) and exhibits the highest average fracture density recognized along the entire KAIF. In tip and intersecting damage zones, damage structures exhibit a larger azimuthal variability and hence a greater fracture connectivity (average number of connections per branch ($C_B$) 1.60 and 1.53, respectively) compared to wall damage zones (average $C_B$ value 0.88). Accordingly, significant along-strike variations of damage zone parameters occur in the absence of a clear dependence on fault displacement. Particularly, fault intersections and tip regions represent areas of enhanced secondary permeability potentially controlling fluid circulation in the subsurface.

## 1. Introduction

Fault zones can act as hydraulic conduits and/or barriers, thus playing a major role in controlling fluid distribution and migration in the crust (Caine et al., 1996; Storti et al., 2003; Roure et al., 2005; Agosta, 2008; Mozafari et al., 2015, 2019; Lucca et al., 2018; Smeraglia et al., 2021; Curzi et al., 2023a, 2023b). The hydraulic properties of fault zones are governed by a number of factors, among which are of particular importance the (i) fault zone architecture, (ii) spatial arrangement of deformation structures and fault-bounded shear lenses characterized by different petrophysical (e.g., permeability-porosity) properties, and, most importantly, (iii) fracture density and connectivity (e.g., Caine et al., 1996; Aydin, 2000; Wibberley et al., 2008; Ceccato et al., 2021; Curzi et al., 2023b). Understanding the factors that control fracture distribution in fault zones and associated damage zones is, therefore, fundamental for the fine-tuning of 2D and 3D models of fractured rock volumes, which, in turn, severely impacts upon the modes of fluid circulation in the upper crust, fault mechanics and the overall comprehension of fractured reservoirs, aquifers, and depleted oilfields for $CO_2$ sequestration and storage (Beach et al., 1999; Roure et al., 2005; Jeanne et al., 2013; Rinaldi et al., 2014; Rohmer et al., 2014; Busch and Kampman, 2018; Aubert et al., 2019).

Fracture density generally decreases according to an exponential or a power law with increasing distance from the fault core (Shipton and Cowie, 2003, 2001; Berg and Skar, 2005; Mitchell and Faulkner, 2009; Savage and Brodsky, 2011; O'Hara et al., 2017; Balsamo et al., 2019; Mayolle et al., 2019; Torabi et al., 2020; Martinelli et al., 2020; Ostermeijer et al., 2020; Ceccato et al., 2021). Many studies indicate that fault displacement is an important factor controlling damage zone thickness and fracture density (e.g., Beach et al., 1999; Shipton and Cowie, 2001; Childs et al., 2009; Mitchell and Faulkner, 2009; Savage and Brodsky, 2011). These general relationships notwithstanding, specific variations of damage zone width and fracture orientation, density, and connectivity down-dip and along-strike can occur without a direct dependence on displacement (e.g., Davatzes et al., 2005; Kirkpatrick et al., 2008; Childs et al., 2009; Storti et al., 2011; Ferrill et al., 2017; Lucca et al.,

* Corresponding author.
*E-mail address:* luigiriccardo.berio@unipr.it (L.R. Berio).

https://doi.org/10.1016/j.jsg.2023.104981
Received 8 June 2023; Received in revised form 6 October 2023; Accepted 13 October 2023
Available online 14 October 2023

2018; Nixon et al., 2020).

Down-dip and along-strike variations in damage zone properties are generally attributed to the evolution of fault zones and different growth modes as function of different rates of displacement accumulation vs. effective fault lengthening (e.g., Nicol et al., 2017; Rotevatn et al., 2018). Fracture studies at different structural positions along faults (for example, at different down-dip and along-strike positions) may contribute to better understand modes and timing of fault growth in space and time and explain the significant heterogeneity in the available displacement-damage zone thickness datasets (e.g., Kim et al., 2004). Different classification and nomenclature schemes have been proposed for fault damage zones (Fig. 1) (e.g., Kim et al., 2004; Choi et al., 2016; Peacock et al., 2017). In particular, Kim et al. (2004) proposed a field-based classification for damage zones according to their structural position along fault zones. They identified wall, tip and linking damage zones. Wall damage zones include rock volumes deformed during displacement accumulation. Tip damage zones consist of rock volumes deformed around a fault tip. Lastly, linking damage zones identify rock volumes damaged in response to the interaction and linkage of fault segments in a relatively small region. Peacock et al. (2017) modified this classification by introducing the concept of interaction damage zones, in turn subdivided in linking, approaching, and intersecting damage zones. Linking and approaching damage zones contain rock volumes deformed due to two or more faults that do not intersect whereas intersecting damage zones consist of rock volumes damaged around the intersection point/line of two or more fault zones (Fig. 1).

Despite several studies on fracturing style associated with complex fault zones (e.g., McGrath and Davison, 1995; Gartrell et al., 2004; Davatzes et al., 2005; Rotevatn et al., 2007; Kirkpatrick et al., 2008; Kim and Sanderson, 2010; Person et al., 2012; Rotevatn and Bastesen, 2014; Nixon et al., 2014, 2019, 2020; Balsamo et al., 2016; Fossen and Rotevatn, 2016; Peacock et al., 2017; Mercuri et al., 2020), only a few publications have documented in detail and quantified the damage zone parameters and how they may vary along- and across-strike, including also fracture connectivity from 2D-network topology. For instance, Lucca et al. (2020), Martinelli et al. (2020), and Hansberry et al. (2021) investigated how topological characteristics vary in the damage zones of regional-scale extensional fault systems accommodating displacements from hundreds to thousands of meters by presenting data from only one fault block (footwall or hanging wall) and from a single across-fault section. Nixon et al. (2020) explored how fracture connectivity varies along-strike in individual fault zones with displacement less than 1.5 m.

In this context, the lack of an extensive evaluation of damage zone parameters along fault systems may impact upon the possibility to produce refined (2D and/or 3D) models of fault architecture, fracture properties, and related implication on geofluid circulation (e.g., Congro et al., 2023; Quevedo et al., 2023). Hence, high resolution studies of damage zone and related fracture networks along entire fault zones (from the tip to the central sectors) are still desirable, as they are central to improve the understanding of damage zone architecture, associated fracture distribution and, above all, of the underlying controlling parameters and processes.

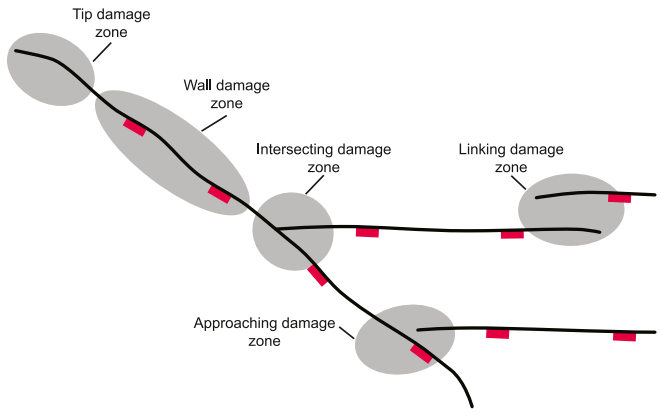


**Fig. 1.** Schematic representation in map view of the different types of damage zones according to the categories defined in Peacock et al. (2017).

On this ground, our aim is to provide a new dataset of damage zone parameters associated with a segmented extensional fault system. In particular, we characterize the across- and along-strike variability of damage zone parameters (i.e., width, fracture density, attitude of damage structures, and fracture connectivity) for three different damage zone types (i.e., wall, tip and intersecting damage zones *sensu* (Fig. 1) Peacock et al., 2017) along the Kornos-Aghios Ioannis Fault (KAIF) on Lemnos Island in the North Aegean Sea of Greece (Fig. 2). The KAIF is a ~10 km long well-exposed extensional fault system that deformed siliciclastic turbidites and volcanic rocks, by accommodating hundreds of meters of extensional displacement at shallow depth (<1 km; Fig. 2). We provide a detailed characterization of the fault system geometry, internal architecture and kinematics, which was preparatory for the selection of across-fault sections to carry out comparative fracture analysis among the three different damage zone types.

## 2. Geological setting

The Aegean region evolved as part of a convergent plate boundary, above the north-dipping Hellenic subduction zone, which produced an orogenic system characterized by the stacking of large tectonic nappes (e.g., Taymaz et al., 2007; Jolivet et al., 2013). Thickened lithospheric domains were affected by syn-to post-orogenic extension (Jolivet et al., 1994, 2018), driven by gravitational instability of the Hellenic orogenic wedge and by the southward migration of the subduction system (Bonev and Beccaletto, 2007; Jolivet and Brun, 2010; Jolivet et al., 2013). In the North Aegean region, Tertiary extension and exhumation were accompanied by widespread igneous activity (Pe-Piper et al., 2009) and by Eocene-Miocene sedimentation in several subsiding depocenters (e.g., Thrace Basin; Siyako and Huvaz, 2007; Innocenti et al., 2009; Caracciolo et al., 2011).

A clastic sedimentary sequence deposited in the western Thrace Basin is well exposed on Lemnos Island, where it includes Middle-Upper Eocene to Lower Miocene deep marine turbidite sandstone (Fissini-Sardes and Ifestia Units) unconformably overlain by shallow marine to continental deposits (Fig. 2) (Therma Unit; Innocenti et al., 1994, 2009; Caracciolo et al., 2011; Maravelis et al., 2015). This Tertiary sedimentary sequence has a maximum stratigraphic thickness of about 500 m and is reported as having experienced only shallow burial (T max <70 °C) (Caracciolo et al., 2011; Perri et al., 2016). It is intruded and partly covered by calc-alkaline to shoshonitic Lower Miocene effusive and hypabyssal magmatic rocks of the Romanou, Katalakkon and Myrina Units (Fig. 2) (Innocenti et al., 2009; Pe-Piper et al., 2009). Pliocene-Quaternary continental deposits locally cover the area (Innocenti et al., 1994, 2009).

Lemnos is located within a seismically active area (e.g., Pavlides et al., 1990, 2009), ~25 km to the south of the North Aegean Trough (NAT), a narrow and highly subsiding ENE-WSW transtensional domain that represents the westward prosecution of the North Anatolian Fault (NAF; Pavlides et al., 1990; Taymaz et al., 1991; Armijo et al., 1999; Koukouvelas and Aydin, 2002). The NAF possibly originated at 10 Ma in eastern Anatolia and entered the Aegean region at 5 Ma (Armijo et al., 1999). ENE-WSW to NE-SW branches of the NAF characterize also the East Aegean Sea 30–40 km to the south of Lemnos as attested to by recent seismicity and strike-slip focal mechanism solutions (Fig. 2) (Pavlides and Tranos, 1991; Caputo et al., 2012; Kiratzi and Svigkas, 2013). Accordingly, Lemnos Island is located within a fault-bounded crustal sliver along the NAF.

The Kornos-Aghios Ioannis Fault (KAIF) is a SW-dipping segmented extensional fault system that has been active since Lower Miocene, prior to and during volcanic activity in the island, in the context of the North

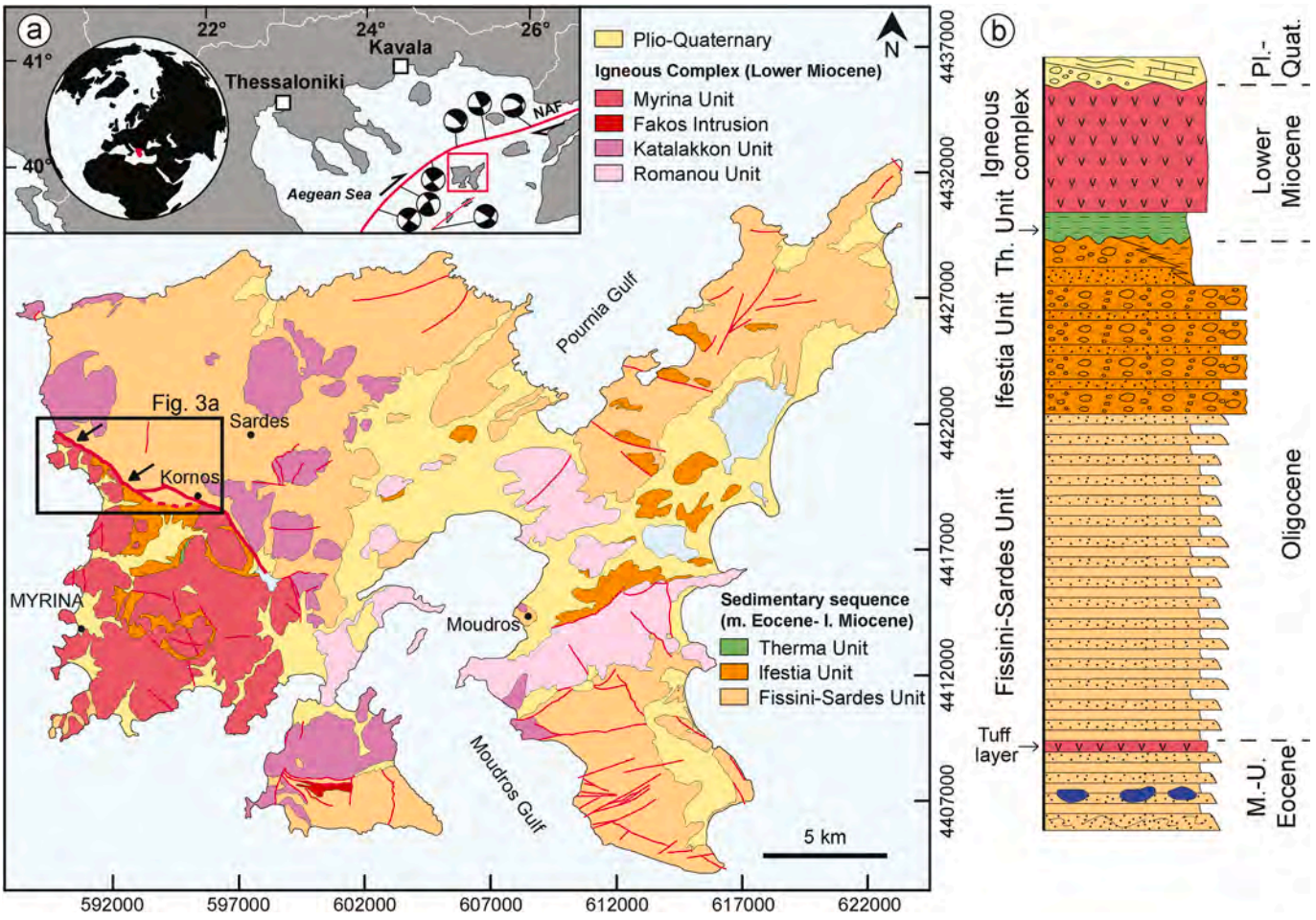


**Fig. 2.** (a) Simplified geological map of Lemnos Island redrawn after Innocenti et al. (1994, 2009). The black square indicates the study area and the black arrows the Kornos-Aghios Ioannis Fault (KAIF). NAF: Northern Anatolian Fault. Focal mechanisms are from Pavlides et al. (1990) and Koukouvelas and Aydin (2002). (b) Stratigraphic column of the Cenozoic units exposed on Lemnos Island redrawn after Innocenti et al. (1994).

Aegean extension and of the related volcanic activity (Innocenti et al., 1994, 2009). It has an onshore total length of ~10 km and a poorly constrained throw of some hundreds of meters (Fig. 2) (Innocenti et al., 2009; Tranos, 2009) that was accommodated at shallow depth, since the deformed stratigraphy experienced only shallow burial (<1 km; Perri et al., 2016). It bounds to the SW a structural low hosting the sediments of the Lower Miocene Therma Unit and separates the Myrina and the Katalakkon volcanic units (Fig. 2) (Innocenti et al., 2009). The KAIF cuts primary igneous contacts and several intrusive bodies that crop out along the fault system, where deformed rock volumes are locally strongly silicified by hydrothermal fluids (Papoulis and Tsolis-Katagas, 2008; Fornadel et al., 2012; Anifadi et al., 2017), particularly in the northwestern portion, with silicification fading away to the SE.

## 3. Methods

### 3.1. Structural analysis

Field work allowed us to reconstruct the overall structural architecture of the KAIF and identify suitable sites for follow-up detailed structural investigations. We systematically collected fault orientation and kinematic data from 37 structural sites that, for convenience, are grouped into 21 stations (Fig. 3a). A total of 502 fault surfaces were measured, out of which 304 exhibits slickenlines and clear kinematic indicators. Statistical analysis of structural data was carried out with Daisy 3 software (Salvini, 2019). Structural data are reported according to the right-hand rule where the dip-direction is to the right of the reported strike azimuth and are shown in lower hemisphere stereographic projections (Schmidt net).

Measured fractures include joints (98.3% of data) and subsidiary faults (1.7% of data) that accommodate centimetre to metre offsets. The occurrence of quartz or calcite veins is sporadic and, hence, they were not included in our dataset. Both joints and subsidiary extensional faults are assumed to be coeval with activity of the KAIF, based on the following geometric and kinematic factors: (i) joints are vertical/sub-vertical throughgoing fractures parallel/sub-parallel to the master fault and to its splays, which is indeed a common feature in cohesive rocks in extensional fault damage zones (e.g., Wagner and Summers, 2005), (ii) the density of both joints and subsidiary faults increases approaching the master fault, as commonly observed in fault damage zones (e.g., Choi et al., 2016), implying that these damage structures are genetically related to the fault, (iii) subsidiary faults exhibit the same kinematics of the closest master fault surfaces.

### 3.2. Fracture density analysis

Fracture density analysis in damage zones was performed by four across-fault linear scanlines (SC1a, SC1b, SC2 and SC3) in different structural sectors (Fig. 3a) to study the fracture patterns in a wall damage zone (scan SC1a and SC1b), a tip damage zone (scan SC2) and an intersecting damage zone (scan SC3 *sensu* Peacock et al., 2017). Scanlines were oriented perpendicular to the master fault direction and to the associated damage structures so as to avoid orientation biases. Whenever possible, we exploited vertical exposures. A total of 1908

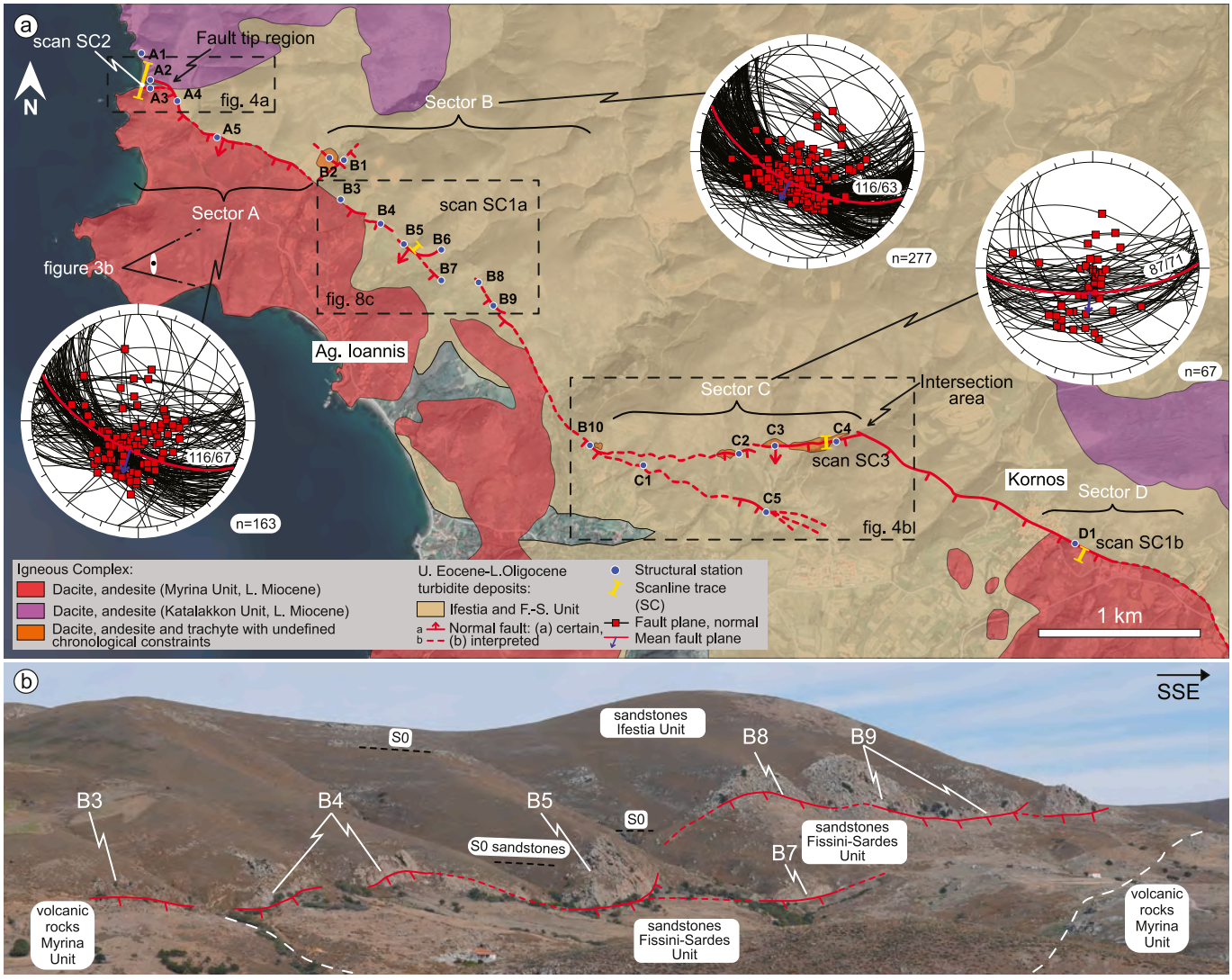


**Fig. 3.** (a) Satellite image of the study area overlain by a simplified geological map redrawn and modified after Innocenti et al., (1994), 2009 (see Fig. 2 for location). The image shows the overall 2D geometry of the KAIF, the locations of scanlines across fault zones (SC1a, SC1b, SC2 and SC3) and structural sites where structural data were collected (A1-A5, B1–B10, C1–C4 and D1). Cumulative stereonets showing the attitude and kinematics of master fault planes in sectors A, B and C are shown. Red squares indicate the orientation of the slickenlines on master fault planes and the normal kinematics. Red great circles represent the mean fault plane for each sector and the blue arrows the mean pitch values. (b) Panoramic view of sector B of the KAIF. (For interpretation of the references to colour in this figure legend, the reader is referred to the Web version of this article.)

joints were measured along the abovementioned scanlines, which altogether cumulate a total length of 265 m. Measured fractures include joints (98.3% of data) and subsidiary faults (1.7% of data) that accommodate centimetre to metre offsets.

In each scanline, the origin of the reference system corresponds to the master fault surface (e.g., Balsamo et al., 2019) with negative and positive values for progressively increasing distances into the footwall and hanging wall, respectively. Along the scanlines, we collected the position of individual joints (i.e., the distance between the origin of the scanline and the intersection between the scanline and the joint) from which we calculated 1D joint density, that is, the number of joints per unit length of scanline ($P_{10}$ expressed in $m^{-1}$). The fracture attitude (strike/dip angle) was also measured. Among the joints that intersect the scanlines, those that were not parallel/sub-parallel to the master KAIF were not considered in order to avoid in the dataset any bias induced by deformation structures formed under a stress regime unrelated to the KAIF extensional faulting. Within fault damage zones, mostly throughgoing joints were sampled. When different rock types are crossed by a single scan line (e.g., in scan SC1), joint density data are presented by adopting different colours for the different lithologies (i.e., volcanic rock, silicified sandstone, not silicified sandstone). Along the four scanlines, also subsidiary fault spacing was measured and corrected for fault dip in order to obtain true spacing values, which are provided as subsidiary fault density in Table 1. The quality of data acquisition reflects outcrop exposure. Locally, we decided to combine several scanline traces to reduce length intervals with poor outcrop quality or no outcrop. The gaps in outcrop exposure (light grey in the graphs) have a total length of 55.35 m out of 265 m (21% of the total sampling length). We analysed joint frequency by bar diagrams with 1 m bin size and gaps >1 m are coloured in grey. In gaps <1 m, joint data are marked as incomplete and indicate the minimum joint frequency for the given bin.

Damage zones boundaries are defined and placed at the change of the slope gradient of the cumulative joint frequency distribution (e.g., Berg and Skar, 2005; Choi et al., 2016). We applied the correction proposed by Choi et al. (2016) for the intervals characterized by no outcrop, in which we inferred joint density by using adjacent slope gradients. Following each gap, we corrected the cumulative joint frequency (corrected data, red circles in the graphs) by adding a certain

**Table 1**
Summary of damage zone parameters in wall, tip and intersecting damage zones including average azimuth of damage structures, damage zone width, average fracture density and the average density of subsidiary faults. DZ, damage zone; FWDZ, footwall damage zone; HWDZ hanging wall damage zone.

| Type of damage zone | Block | Damage zone subdomain | Average azimuth of damage structures (±st. dev.) | Width of subdomain (m) | Width of FWDZ/ HWDZ (m) | Total width (m) | Average joint density ($m^{-1}$) | Average subsidiary faults density ($m^{-1}$) | Lithology |
|---|---|---|---|---|---|---|---|---|---|
| **Wall DZ** (Scan 1a-1b) Fig. 9 | FWDZ | Inner DZ | 83.88°W±11.52° | 4.1 | 26 | 72.6 | 17 | 0.05 | Silicified sandstones |
| | | Outer DZ | | 21.3 | | | 6.3 | | Silicified sandstones |
| | HWDZ | Inner DZ | 66.50°W±9.12° | 10.2 | 46.6 | | 7.4 | | Volcanic rocks |
| | | Outer DZ | | 36.4 | | | 5.5 | | Volcanic rocks |
| **Tip DZ** (Scan 2) Fig. 10 | FWDZ | Inner DZ | 67.99°W±18.48 | 6.5 | >82 | >122 | 18.4 | 0.26 | Silicified/not silicified sandstones |
| | | Outer DZ | | 75.5 | | | 11.5 | | Silicified/not silicified sandstones/volcanic rocks |
| | HWDZ | Inner DZ | | 7.6 | >40 | | / | | Volcanic rocks |
| | | Outer DZ | | 32.4 | | | 9.7 | | Volcanic rocks |
| **Intersecting DZ** (Scan 3) Fig. 11 | FWDZ | Inner DZ | 89.40°W±21.07° | 5.2 | 19.9 | 50.9 | 5.6 | 0.13 | Volcanic rocks |
| | | Outer DZ | | 14.7 | | | 3.8 | | Volcanic rocks |
| | HWDZ | Inner DZ | | 5.7 | 31 | | 16.1 | | Volcanic rocks |
| | | Outer DZ | | 25.3 | | | 10.4 | | Volcanic rocks |

amount of joints for the interval characterized by no outcrop or poor outcrop quality. To do that, for the intervals with no outcrop we assumed the same rate of increase (i.e. the same slope of the trend line) calculated for the data interval that precedes the gap. If the scanline starts with a gap (i.e. no data precede the gap), data correction in the first gap was made by considering the same rate of increase of the corresponding interval (i.e. same distance from the master fault) in the other fault block (footwall or hanging wall).

At a distance >150 m from the master fault, we quantified background deformation in three different along-strike sectors(sector A, B and C; Fig. 3a). The critical value of at least 150 m from the master fault was defined conservatively as to exclude any possible influence of the fault. To define this value, we considered the estimated KAIF throw in the order of hundreds of meters (200–300 m; Innocenti et al., 2009) and the displacement-thickness correlations (Torabi and Berg, 2011). The background fracture density was determined by performing 5–8 m long linear scanlines oriented approximately perpendicular to the structures on vertical or horizontal exposures. Along the scanlines, the number of fractures/m was counted and for each scanline we calculated the 1D fracture density ($P_{10}$ expressed in $m^{-1}$).

### 3.3. Fracture topology analysis

Topological analysis was run for each fault damage zone (i.e. wall, tip, and intersecting damage zones; Sanderson and Nixon, 2015, 2018). The topology of a 2D-fracture network consists of lines, nodes, and branches, with each line consisting of one or more branches with nodes at their terminations (Sanderson and Nixon, 2015). Nodes are classified in 3 types: I nodes represent isolated tips, Y nodes the point of abutting or splaying of fractures, X nodes the intersection point of crossing fractures. Consequently, X and Y nodes are connecting nodes, whereas I nodes are isolated. Branches are classified into three types considering whether the nodes at their terminations are connecting (C) or isolated (I): isolated branches (II), partially connected (CI) and fully connected (CC). In the branch counting process, a branch that entirely falls within the sampling area counts as 1 whereas a branch that is only partially within the sampling area may count as 0.5 or 0 depending whether one endpoint or both endpoints are outside the sampling area, respectively (Nyberg et al., 2018). Where branches fall only partially within the sampling area, branch classification is made considering also the nodes outside the sampling area (Nyberg et al., 2018). The proportions of node and branch types are plotted on ternary diagrams in order to topologically characterize the fracture network (i.e., Sanderson and Nixon, 2015). To analyse the degree of fracture network connectivity, two parameters have been calculated and are represented by the *connections per branch* ($C_B$), which describes the degree of connectivity between branches (Sanderson and Nixon, 2015), and the *average degree* (<D>), which describes the degree to which nodes are connected to branches (Sanderson et al., 2019; Nixon et al., 2020):

$$C_B = \frac{3N_Y + 4N_X}{B} \quad (1)$$

$$\frac{B}{N} = < D > \Big/ 2 \quad (2)$$

where $B$ and $N$ are the number of branches and nodes, respectively, and $N_Y$ and $N_X$ the number counts of Y and X nodes, respectively. The value of $C_B$ can vary between 0 and 2, where 0 represents a totally disconnected network and 2 a fully connected network. The $C_B$ parameter is contoured onto both the branch and node ternary diagrams. The value of $<D>$ varies between 1 (poorly connected branches dominated by I nodes and II branches) and 4 (completely connected network dominated by X nodes and CC branches).

Thirteen circular scan areas were defined and studied on photographs acquired with a Leica D-Lux 7 camera. Scan areas were selected on across-fault scanlines (SC1a, SC1b, SC2, SC3) exploiting vertical exposures roughly perpendicular to the master fault trend. The positions along scanlines were selected as a compromise between best outcrop quality and the necessity to characterize both inner and outer fault damage zones while assessing across-fault spatial variability of the topological parameters. A diameter of 1 m was imposed by the quality of the outcrops since larger diameters would have included vegetation or detritus. Photographs were imported in QGis and the Network GT toolbox (Nyberg et al., 2018) was used to extract topological information from manually digitized fracture networks. In addition to I, X, and Y nodes, Network GT toolbox also identifies the points where fractures intersect the sampling area (referred to as E nodes - edge nodes). However, E nodes are not considered in the total node counts and in the calculations of the connectivity parameters. A total of 1308 fractures was digitized including all the fractures in the scan areas irrespectively of their orientation.

## 4. Results

### 4.1. Fault architecture in map view

The KAIF includes two major overlapping fault segments oriented ~ NW-SE: a northern one (sector A and B) and a southern one (sector D). These two segments are connected by an E-W breaching fault (sector C) (Fig. 3a). The hanging wall of the KAIF consists of Tertiary turbidites of

the Ifestia Unit with local hypabyssal intrusions of the Myrina Unit (Fig. 3a–b). In the footwall, Tertiary turbidites of the Fissini-Sardes Unit and dacites/andesites of the Katalakkon Unit crop out (Fig. 3a–b).

The northern fault segment (sectors A, B and C) extends for about 4 km from site A1 to site C5, where the fault zone dies out into several splays (Fig. 3a). In the northwestern portion of sector A, the KAIF tip region is exposed (tip damage zone) and is characterized by curved fault splays that form a horse tail geometry (Figs. 3a and 4a). Overall, this fault segment is partially to intensely silicified, thus creating a positive relief due to the erosional contrast with respect to the non-silicified country rocks (Fig. 3b). The silicified volumes are thicker in the fault tip region of sector A and become progressively thinner moving southeastward in sector B. The connecting E-W segment extends for about 1.5 km from site B10 to site C4 and is poorly or not silicified (Figs. 3a and 4b). The eastern portion of this E-W fault zone is a linkage area between two main intersecting fault segments with different orientation (intersecting damage zone; site C4 in Figs. 3a and 4b). The southern NW-SE fault segment (sector D) is about 3 km long and is not silicified. There, the master slip surface is generally poorly exposed as it is generally covered by vegetation. Therefore, in sector D the fault trace was mapped following (i) the contact between the Myrina and the Fissini-Sardes Unit (Fig. 3a), (ii) the normal drag in the sandstones, and (iii) a general joint density increase within the fault damage zone. The mean attitude of master fault surfaces in the sectors A, B and C is 116/67 (n = 163), 116/63 (n = 277) and 87/71 (n = 67), respectively (stereonets in Fig. 3a). Slickenlines indicate predominant dip-slip motions in all the segments, with mean pitch values of 85.6° ± 19.3 (n = 94), 92.2° ± 14.4 (n = 207) and 93.4° ± 17.1 (n = 43), respectively (Figs. 3a, 4a-b).

At a closer view, the two NW-SE fault segments and the E-W connecting one are highly segmented and segments have length in the range of 40–200 m (Figs. 3a–b, 5a). Fault segments overstep along-strike (e.g., between structural sites B4–B5 and B7–B8) and, locally, abruptly bend to form curved fault strands (e.g., site B6) (Figs. 3a–b, 5a). In sector A-B, very well-preserved silicified fault scarps mark the position of the master fault over a length of 4.2 km (Figs. 3b, 5a-b).

### 4.2. *Fault zone structure in cross section*

The fault zone structure consists of a ~m-thick fault core surrounded by a fractured damage zone developed both in the hanging wall (HWDZ) and in the footwall (FWDZ). Master fault surfaces have striae and grooves indicating dip-slip movements (Figs. 5b and 6a). Discrete master

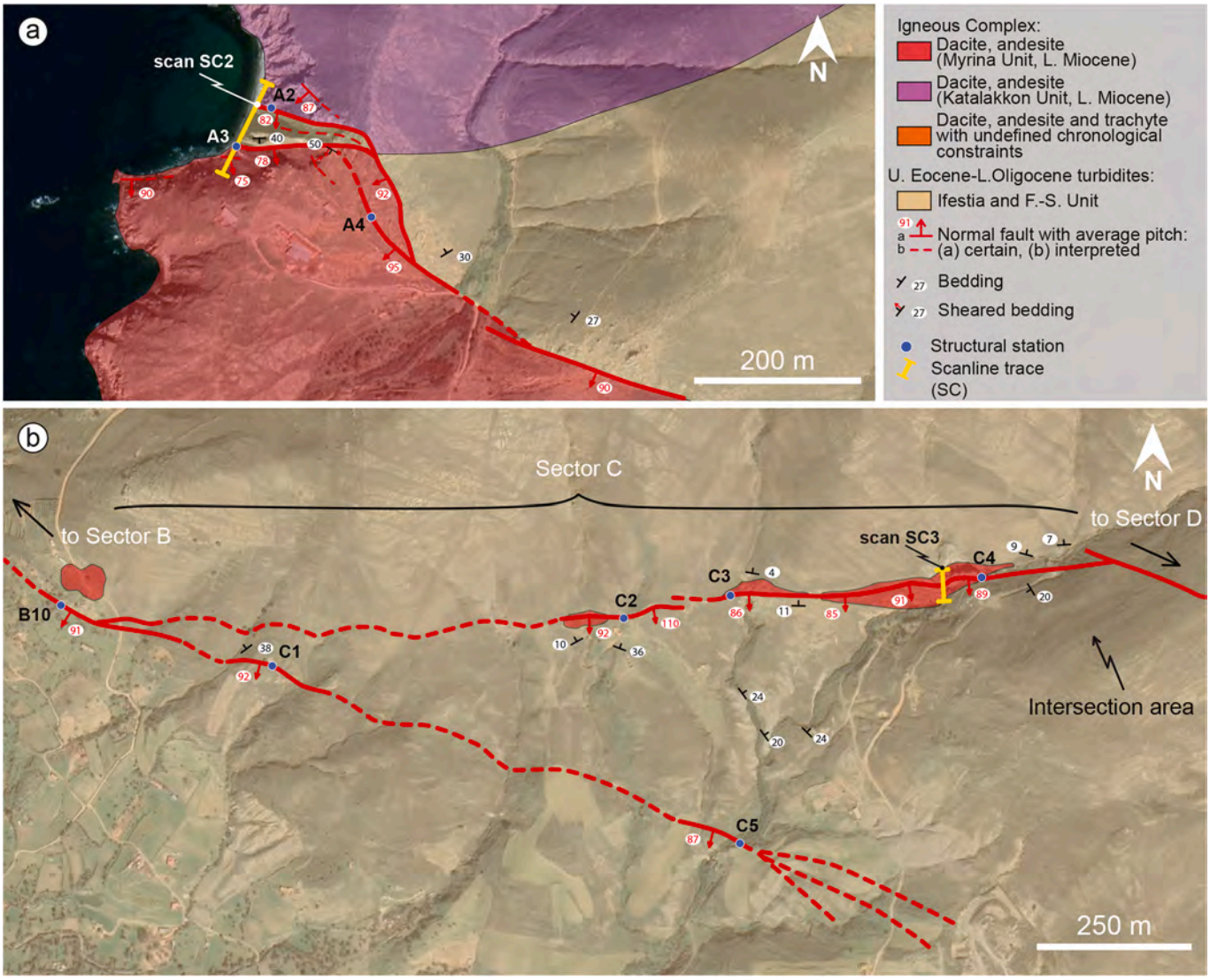


**Fig. 4.** Satellite images overlain by a simplified geological map redrawn and modified after Innocenti et al. (1994, 2009) (see Fig. 3a for location) showing the master fault segments and their kinematics, the studied structural sites, the attitude of bedding planes and the location of across-fault scanlines. (a) Tip damage zone of sector A. (b) Intersecting damage zone of sector C.

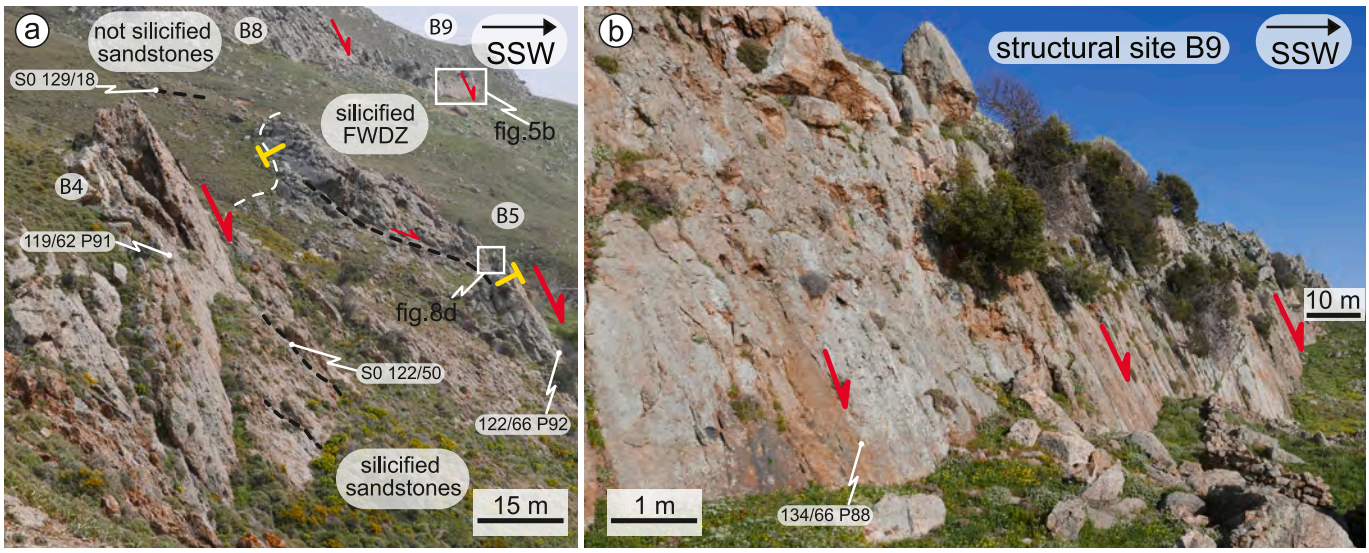


**Fig. 5.** (a) Cross-fault panoramic view of the segmented fault zone of sector B showing the master fault plane and the footwall damage zone at structural site B5. Bedding planes (dashed black lines) are progressively dragged approaching the master fault plane both in the hanging wall and in the footwall consistently with the normal kinematics. The dashed white line indicates the maximum extension of silicified sandstones in the footwall of the KAIF. Yellow marks indicate the starting/ending point of scanline SC1a that crosses an example of footwall wall damage zone. (b) Panoramic view of the master fault plane at structural site B9. (For interpretation of the references to colour in this figure legend, the reader is referred to the Web version of this article.)

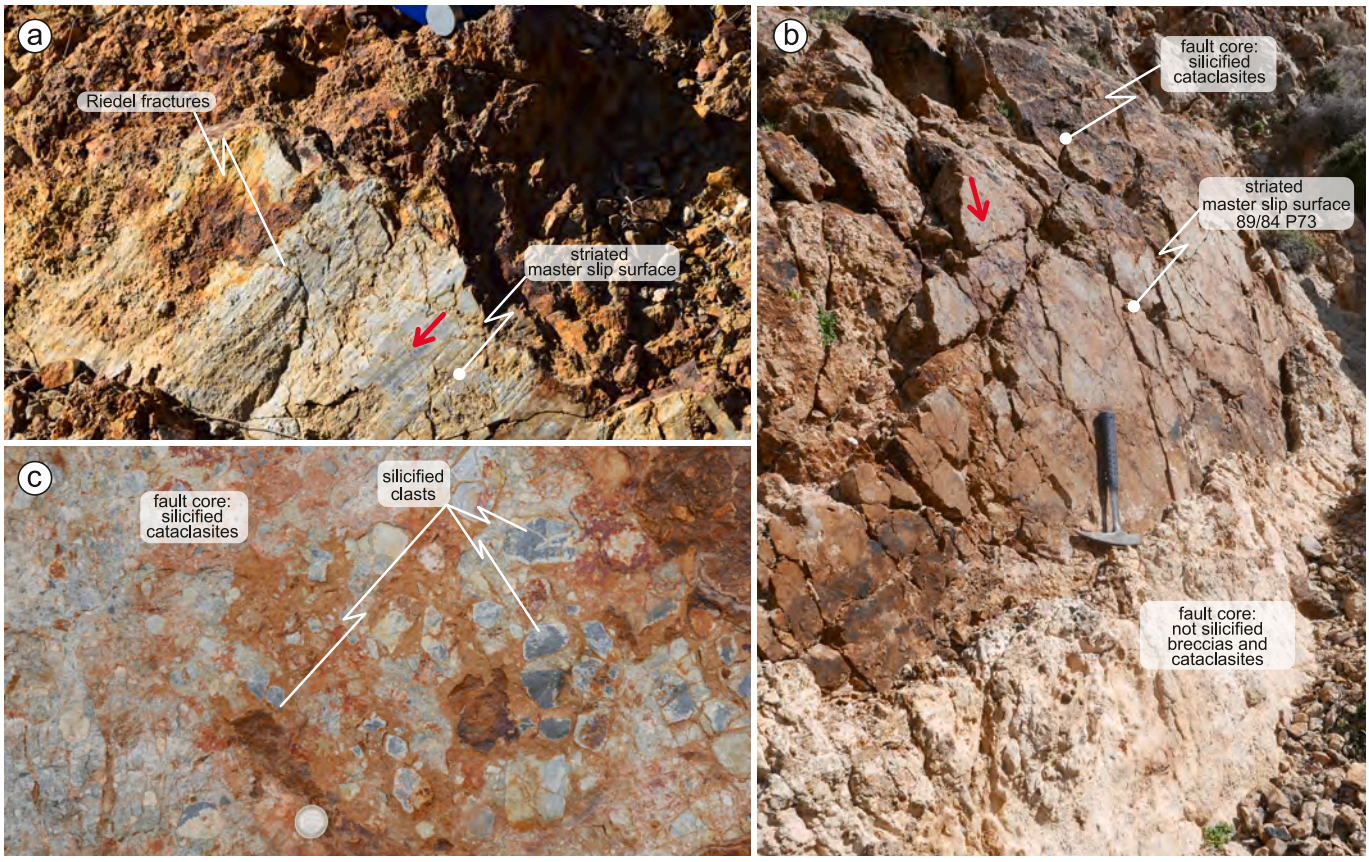


**Fig. 6.** Outcrop images of the principal slip surface and of the fault core. (a) Master fault surface dip-slip striated. Note compass for scale. (b) Master fault surface and fault core. The fault core is made up of cataclasites strongly silicified and not silicified breccias/cataclasites. The red arrows indicate the direction of slip. (c) Detail of the silicified cataclasites of the fault core. Coin for scale. (For interpretation of the references to colour in this figure legend, the reader is referred to the Web version of this article.)

slip surfaces envelope up to 2-m thick fault cores that include incohesive (not silicified) and cohesive (silicified) breccia and cataclasite (Fig. 6b–c).

Damage zones contain synthetic and antithetic subsidiary extensional faults and joints that invariably cut across the silicified and non-silicified sedimentary and volcanic rocks (Fig. 7a). The occurrence of

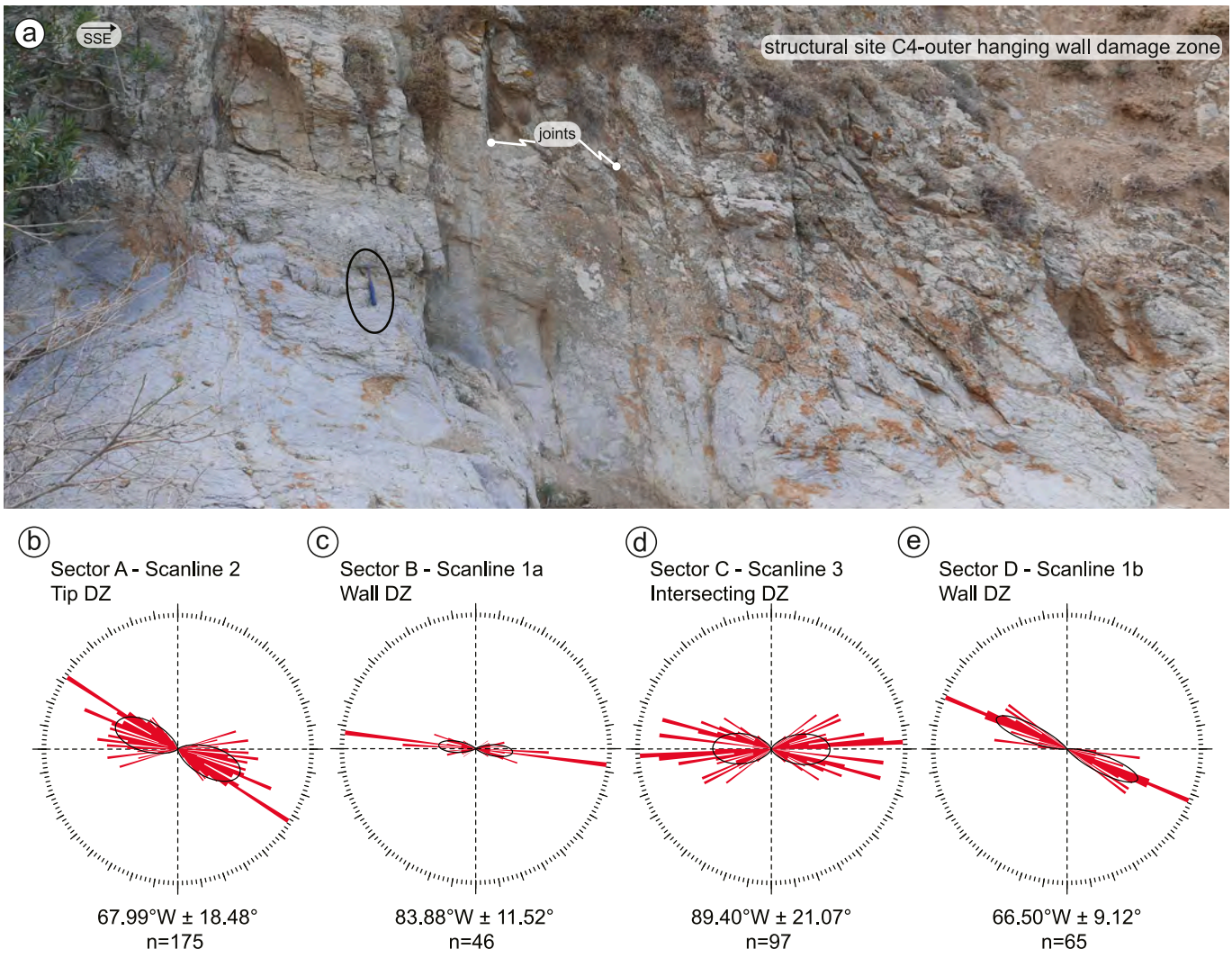


**Fig. 7.** (a) Outcrop image of an outer damage zone affecting volcanic rocks at structural site C4. Hammer for scale in the black circle. (b–e) Rose diagrams showing azimuthal data of damage structures, namely subsidiary faults and joints. (b) Sector A, tip damage zone. (c) Sector B, footwall wall damage zone. (d) Sector C, intersecting damage zone. (e) Sector D, hanging wall wall damage zone. Average azimuth values are reported with their standard deviations.

quartz or calcite veins is sporadic. In FWDZs, the Fissini-Sardes sandstone exhibits crackle to mosaic breccias cemented by milky quartz. In each fault segment, joints are sub-vertical and sub-parallel to the mean strike of the master fault surfaces (Fig. 7). In detail, joints in sector A strike 67.99°W ± 18.48, in sector B strike 83.88°W ± 11.52°,in sector C strike 89.40°W ± 21.07° and in sector D strike 66.50°W ± 9.12° (Fig. 7b–e). It is worth noting that, in the extensional tip region (tip damage zone, sector A) and in the sector between two intersecting segments (intersecting damage zone, eastern sector C), joints exhibit a larger azimuthal variability (i.e., higher standard deviations) than in the wall damage zones (sector B and D; Fig. 7b–e). However, where fractures with different orientations intersect, no systematic crosscutting/abutting relationships were recognized.

Away from fault damage zones, at a distance >40–120 m from the master slip surfaces, bedding planes in turbidite sandstones gently dip 8–38° towards N-NW (mean attitude 234/08) both in the hanging wall and in the footwall (Fig. 8a). Approaching master fault surfaces, turbidite beds in the footwall are progressively dragged consistently with the extensional fault kinematics becoming sub-parallel in proximity of the master fault plane and being frequently exploited as shear planes as attested to by dip-slip slickenlines (Fig. 8b–e).

### 4.3. Background fracture density

At each locality (sector A, B and C), 3 to 5 scanlines were performed and by averaging the fracture density values a value for each measuring site was obtained. Background fracture density in the three different sectors is: 6.5 $m^{-1}$ in sector A, 3.6 $m^{-1}$ in sector B and 2.3 $m^{-1}$ in sector C. The mean background fracture frequency is 4.2 $m^{-1}$.

### 4.4. Joint density data in fault damage zones

#### 4.4.1. Wall damage zone

Due to the lack of continuous outcrop across the northern (sector A, B and C) and southern (sector D) fault segments, data from the wall damage zones stem from the combination of two distinct scanlines located in the footwall of the northern fault segment (sector B; SC1a) and in the hanging wall of the southern one (sector D; SC1b; Fig. 3a). Both scanlines are made up of multiple, subparallel scan traces. Scanline SC1a is within the strongly silicified sandstone and crackle breccia, while scanline SC1b in the dacite of the Myrina Unit (Fig. 9a). Combining both scanlines to produce a representative scanline for the wall damage zone (SC1), produced a cumulative length of 88 m and a total of 474 fracture data (Fig. 9a). The density of subsidiary faults calculated on the entire scanline length is 0.05 $m^{-1}$ (Table 1).

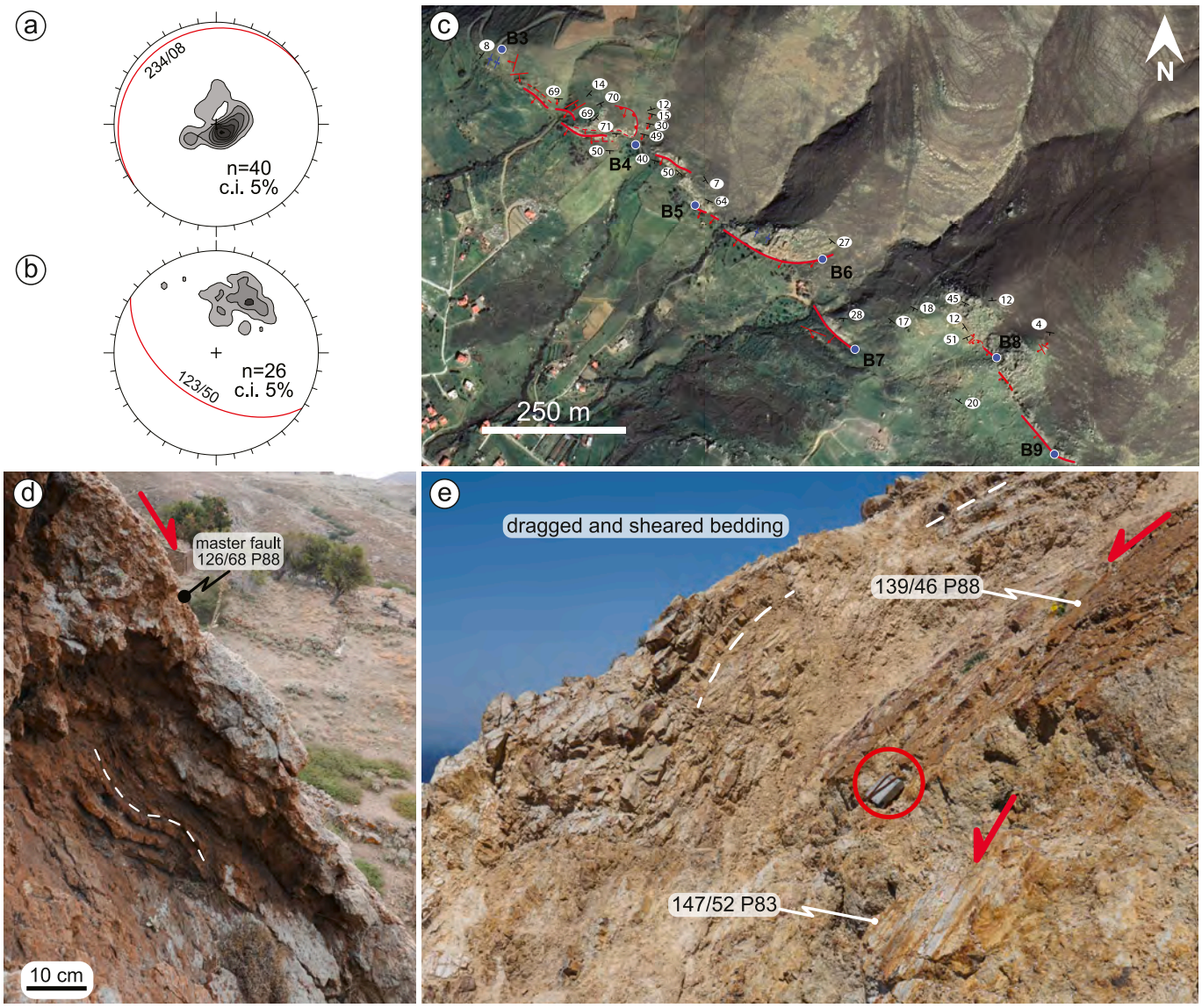


**Fig. 8.** (a–b) Contoured poles to bedding planes of turbidite sandstones of the Ifestia Unit. Red great circles represent the modal bedding plane. (a) Bedding plane attitudes out of fault damage zones (distance >40–120 m from the master fault). (b) Bedding plane attitudes inside HWDZs and FWDZs. (c) Satellite image of sector B (refer to Fig. 2 for the exact location) with indicated the master fault segments (red lines), the structural sites (B3–B9) and the attitude of bedding planes. (d) Bedding surfaces in the inner FWDZ at structural site B6. Turbidite beds in the footwall are progressively dragged consistently with the extensional fault kinematics. (e) Example of dragged and sheared bedding with dip-slip striations in the FWDZ of structural site A3. Note compass for scale in the red circle. (For interpretation of the references to colour in this figure legend, the reader is referred to the Web version of this article.)

Joint density values are plotted against the cross-sectional distance from master slip surfaces in Fig. 9b. In both footwall and hanging wall, joint density tends to decrease moving away from the master slip surface to values corresponding to the background deformation values following a rather irregular trend. Positive fluctuations of density values in the footwall are localized near subsidiary faults, while positive peaks in the hanging wall correspond to clustered joints.

According to the slope gradient of the cumulative joint frequency plots, three subdomains can be identified in both the footwall and hanging wall: an inner damage zone, an outer damage zone and the background (Fig. 9b). The inner footwall damage zone boundaries are located at −4.1 m and at 10.2 m in the footwall and hanging wall blocks, respectively (Fig. 9a and b). The mean joint densities in the inner footwall and hanging wall damage zones are 17 $m^{-1}$ and 7.4 $m^{-1}$, respectively (Fig. 9b, Table 1). The outer damage zone boundaries for the footwall and hanging wall are located at −26 m and at 46.6 m, respectively (Fig. 9a and b). The mean fracture densities in the outer footwall and hanging wall damage zones are 6.3 $m^{-1}$ and 5.5 $m^{-1}$, respectively (Fig. 9b, Table 1). It is worth noting that the slope gradients of the outer damage zones are similar (Fig. 9b). However, the thoroughgoing fault-related joints in sector B (silicified sandstones and crackle breccias) are less persistent than in sector D (dacites) (Fig. 9c and d). In summary, (i) the total width of the wall damage zone is 72.6 m, (ii) the damage is roughly symmetrically distributed close to the fault core, with the hanging wall damage zone wider than the footwall damage zone (46.6 m versus 26 m), and (iii) the damage density in the silicified sandstone in the footwall is higher than in the non-silicified hanging wall dacite (Table 1).

#### 4.4.2. *Tip damage zone*

Scanline 2 (SC2) is located in sector A and, more specifically, at the northwestern exposure of the KAIF tip zone, where the fault is characterized by multiple fault splays forming a horse-tail geometry (Figs. 3a and 4a). SC2 is the result of the combination of several subparallel

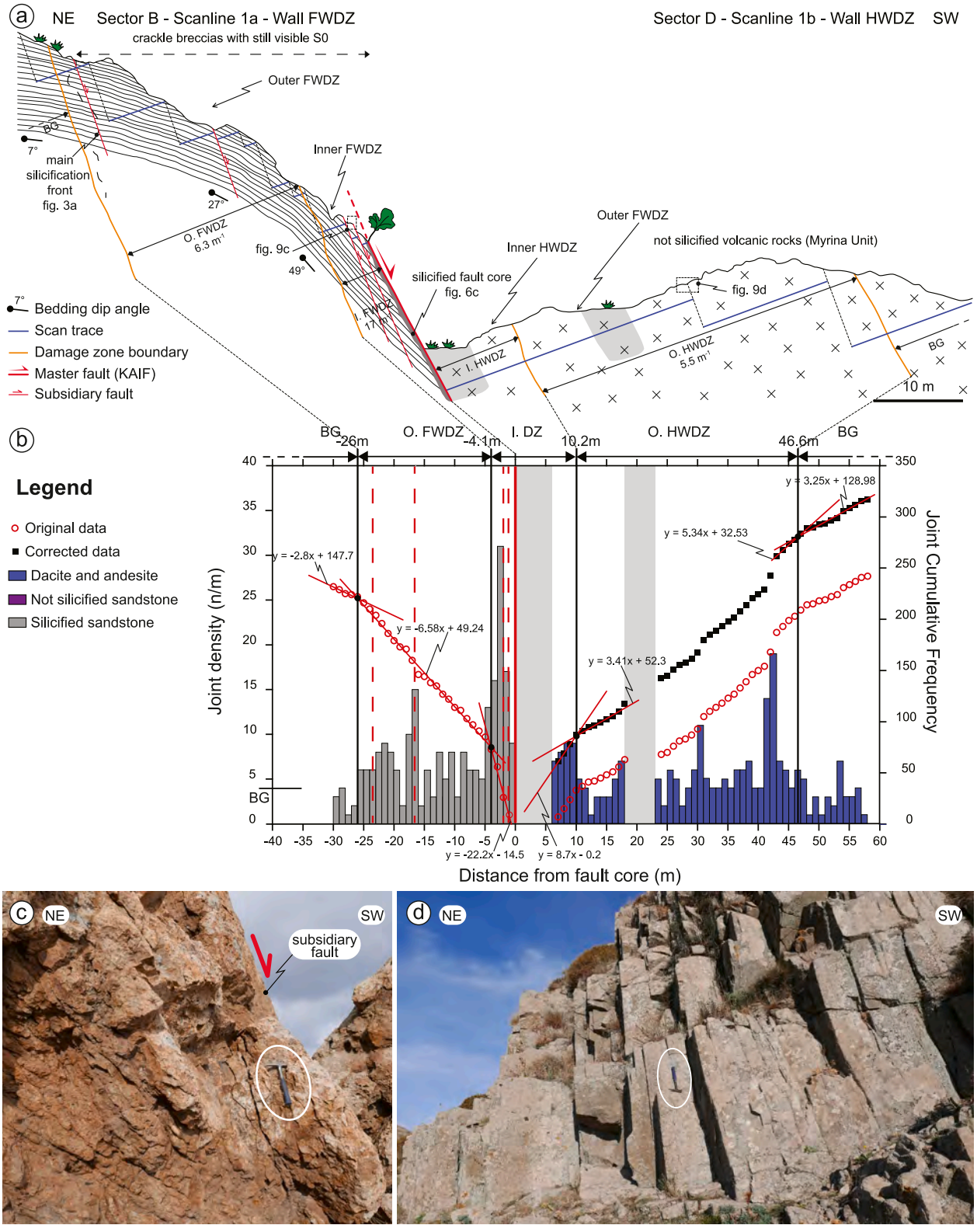


**Fig. 9.** (a) Schematic representation of structural sites B5 and D1 showing the scan line traces that cross the wall damage zones of sector B and D (SC1a and 1b). (b) Joint density vs. distance from fault core plot. Normal frequency as bar diagrams, cumulative frequency as red empty dots (original data) and black squares (corrected data). Dashed red lines are subsidiary normal faults. The colours of the bars indicate different lithologies (see the legend of previous figures for details). O. FWDZ Outer Footwall Damage Zone; I. DZ Inner Damage Zone; O. HWDZ Outer Hanging wall Damage Zone; BG stands for mean background fracture frequency (4.2 $m^{-1}$). (c) Outcrop photograph showing joints and subsidiary faults affecting sandstones and crackle breccias in the inner fault damage zone at structural site B5. (d) Outcrop photograph showing joints in the outer hanging wall fault damage zone (O. HWDZ) at structural site D1. See the sketch of Fig. 11a for the location of the photographs. (For interpretation of the references to colour in this figure legend, the reader is referred to the Web version of this article.)

scanline segments measured at slightly different elevations so as to minimize the intervals with poor outcrop quality or no outcrop (Fig. 10a). Two main fault surfaces are intersected by the scanline: the master fault surface at 0 m (089/84, pitch 73), and a second fault zone in the footwall, at −51 m (132/57 pitch 79) (Fig. 10a). Furthermore, in both footwall and hanging wall, there are several subsidiary extensional faults with offset <5 m, which contribute to the high structural complexity of the KAIF tip. The two main fault surfaces bound a ~50 m thick slice of sandstone in tectonic contact with the Katalakkon Unit to the north, and with the Myrina Unit to the south (Figs. 4a and 10a). Although the sandstone in the tectonic slice is variably bleached and fractured, bedding is still recognizable (Figs. 4a and 10a). It is dragged and brecciated close to the master fault surface. The sandstone in the footwall is irregularly silicified near the master fault surface, thus forming fault-parallel slices of silicified sandstones with a thickness of 5–20 m (Fig. 10a).

SC2 has a total length of 122 m for a total of 1015 measured fracture data. The density of subsidiary faults calculated for the entire scanline length is 0.26 $m^{-1}$ (Table 1). In the bar diagram of the scanline, joint density shows several peaks in the inner and outer damage zones, which are associated with the position of subsidiary faults (Fig. 10b, d). In the footwall, the profile of corrected data is characterized by two distinctive domains with different slopes that allow us to identify an inner footwall damage zone boundary at −6.5 m. The density of joints in the inner footwall damage zone ranges between 9 and 35 $m^{-1}$ (mean density 18.4 $m^{-1}$; Fig. 10b, Table 1). The outer footwall damage zone, which extends to −82 m, has a density of joints ranging between 6 and 27 $m^{-1}$ (mean density 11.5 $m^{-1}$; Fig. 10b, Table 1). In the hanging wall, the lack of outcrop in the interval 0–7 m does not allow an accurate determination of the inner damage zone boundary. However, by maintaining the same slope of the footwall inner damage zone, the boundary can be inferred to be at 7.6 m (Fig. 10b). The outer hanging wall damage zone extends for 40 m from the fault master slip surface, with the joint density varying between 2 and 23 $m^{-1}$ (mean density 9.7 $m^{-1}$; Fig. 10b, Table 1).

In the outer damage zones, linear regressions of the scattered corrected data exhibit different slope gradients, which are steeper in the footwall than in the hanging wall. Generally, in the outermost sectors of SC2, joint density data do not show a systematic decrease down to background values, even excluding second order variations related to subsidiary faults (background fracture density 6.5 $m^{-1}$ in sector A). The entire section covered by SC2 therefore belongs to the fault damage zones and 122 m is the minimum damage zone width in the tip region of sector A. In summary, (i) deformation is less localized near the master fault and appears to be more distributed than in wall damage zones, (ii) local joint density fluctuations occur near secondary faults, (iii) deformation density is slightly higher in the footwall than in the hanging wall damage zone (Table 1).

#### 4.4.3. Intersecting damage zone

Scanline 3 (SC3) is located in the linkage area between two main intersecting fault segments oriented NW-SE and E-W (i.e. intersecting damage zone; sector C; Figs. 3a and 4b). Unlike the cross sections covered by SC1 and SC2, scanline SC3 is not characterized by significant lithological variability, which consists of hypabyssal rocks intruded in unsilicified sandstone (Fig. 11a). SC3 has a total length of 55 m with a total of 419 measured fractures. The density of subsidiary faults calculated on the entire scanline length is 0.13 $m^{-1}$ (Table 1). Overall, joint density is higher in the hanging wall than in the footwall damage zone, and local positive fluctuations are localized in correspondence of subsidiary extensional faults. In the bar diagram, there is a good match between the position of subsidiary faults and the peaks of joint density (Fig. 11b).

In the hanging wall, two distinct slope changes of the cumulative frequency distribution can be recognized. The first occurs at 5.7 m and represents the inner damage zone boundary (Fig. 11b). The density of joints in the hanging wall inner damage zone ranges between 8 and 28 $m^{-1}$ (mean density 16.1). The second represents the outer hanging wall damage zone boundary and is located at 31 m. The density of joints in the hanging wall outer damage zone is in the range between 6 and 22 $m^{-1}$ (mean density 10.4 $m^{-1}$; Fig. 11b, Table 1). In the footwall, three sectors can be identified from the slope gradient pattern. The first one starts at 0 and ends at −5.2 m and corresponds to the inner damage zone, characterized by joint density in the range between 4 and 9 $m^{-1}$ (mean density 5.6 $m^{-1}$). The second one ends at −19.9 m and corresponds to the outer footwall damage zone, where joint density is in the range between 0 and 8 $m^{-1}$ (mean density 3.8 $m^{-1}$; Fig. 11b, Table 1). It is worth noting that the slope gradients of the hanging wall and footwall damage zones covered by SC3 are markedly different, with the former being much steeper than the latter (this is valid for both the inner and outer subdomains). In summary, in the intersecting damage zone, which affects volcanic rocks, (i) the total damage zone width is 50.9 m, (ii) deformation density is much higher in the hanging wall than in the footwall damage zone, and (iii) deformation density has local fluctuations close to subsidiary faults (Fig. 11b, Table 1).

### 4.5. Fracture topology in fault damage zones

The results of the topological analysis are summarized in Table 2 and in Fig. 12, where a quantitative comparison between outer and inner damage zones, and between wall, tip and intersecting damage zones is provided. Outer wall damage zones (scan areas 1 and 4) are dominated by isolated nodes (average $P_I$ 88.17%), by the absence of cross-cutting fractures (average $P_X$ 0%), and by few abutting fractures (average $P_Y$ 11.83%). In the inner wall damage zones (scan areas 2 and 3), the proportions of Y and X nodes increase compared to the outer damage zones (average $P_X$ 3.25% and $P_Y$ 29.50%; Fig. 12a). Outer intersecting damage zones (scan areas 10 and 13) are characterized by an average $P_X$ of 12.05, $P_Y$ of 26.68% and $P_I$ of 61.28%. In the inner intersecting damage zones (scan areas 11 and 12), the proportion of Y nodes increases with respect to the outer sectors (average $P_Y$ 58.34%; Fig. 12c). In summary, in wall and intersecting damage zones, the inner damage zones exhibit a greater proportion of connecting nodes (X and/or Y nodes) with respect to outer damage zones. Therefore, inner damage zones plot closer to the CI-CC axis of the branch triangle than outer damage zones. This difference in terms of branch proportions between inner and outer subdomains is more pronounced for wall damage zones than for intersecting damage zones (Fig. 12a–c).

The difference in node and branch proportions between inner and outer subdomains is not observed in tip damage zones (Fig. 12b). Three scan areas out of four (scan areas 5, 8 and 9) in the outer tip damage zones exhibit a proportion of connecting nodes approximately equal to that of the inner subdomain (scan area 7; Fig. 12b). This high proportion of connecting nodes in the outer sectors is caused by the presence of several subsidiary faults with their own damage structures (e.g., scan areas 5, 8 and 9). Among the scan areas in the outer sectors (5, 8 and 9), the highest proportion of connecting nodes pertains to scan area 5, which is located close to the master fault surface, and represents the tectonic contact between bleached sandstone and andesite, delimiting towards NNE the tectonic slice (Figs. 10 and 12b). In summary, the tip damage zone is dominated by IC and CC branches, and thus plots close to the CI-CC axis of the branch triangles irrespective of the distance from the fault core (Fig. 12b).

In terms of fracture network connectivity, the differences in the proportions of nodes and branches control the *connections per branches* parameter ($C_B$), with the inner damage zones having on average higher $C_B$ values (average $C_B$ 1.50) than outer damage zones (average $C_B$ 1.27) (Fig. 12d). However, as for the proportions of nodes and branches, no substantial differences in $C_B$ values are observed between different subdomains (outer and inner) in the tip damage zone (average $C_B$ 1.60) (Fig. 12b, Table 2). By comparing damage zone along-strike, our results show that intersecting and tip damage zones plot closer to the Y and X node corners of the node triangle and to the CI-CC axis of the branch

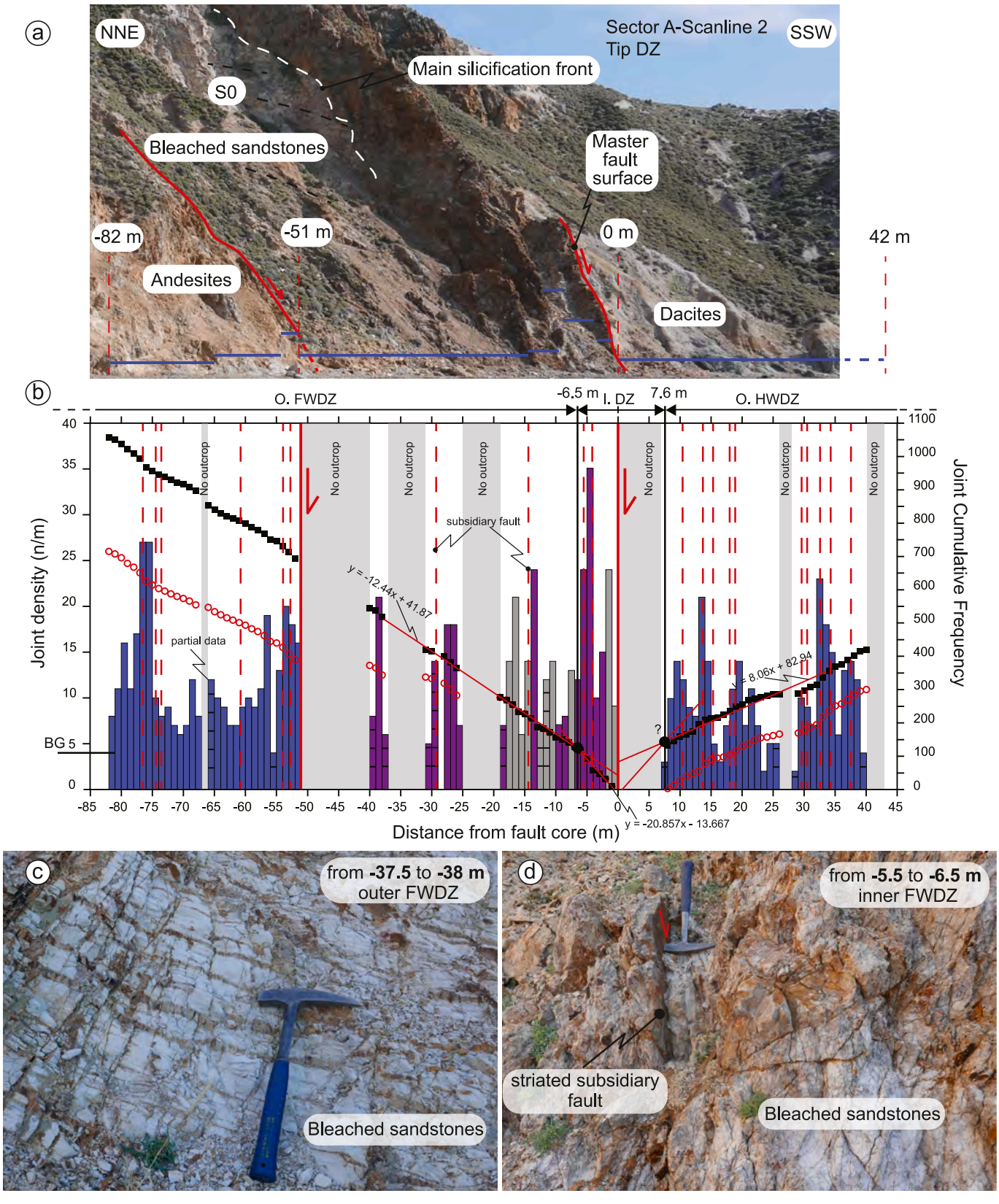


**Fig. 10.** (a) Photograph of the outcrop at structural site A2-A3 showing the scan line traces that cross the tip damage zone of sector A (SC1). The photograph is aligned with the underlying graph. (b) Joint density vs. distance from fault core plot. Normal frequency as bar diagrams, cumulative frequency as red empty dots (original data) and black squares (corrected data). Dashed red lines are subsidiary normal faults. The colours of the bars indicate different lithologies (see the legend for details). Acronyms as in previous figure. (c) Fractured bleached sandstones in the outer footwall damage zone (O. FWDZ). (d) Dip-slip striated subsidiary fault in the inner footwall fault damage zone (I. FWDZ). (For interpretation of the references to colour in this figure legend, the reader is referred to the Web version of this article.)

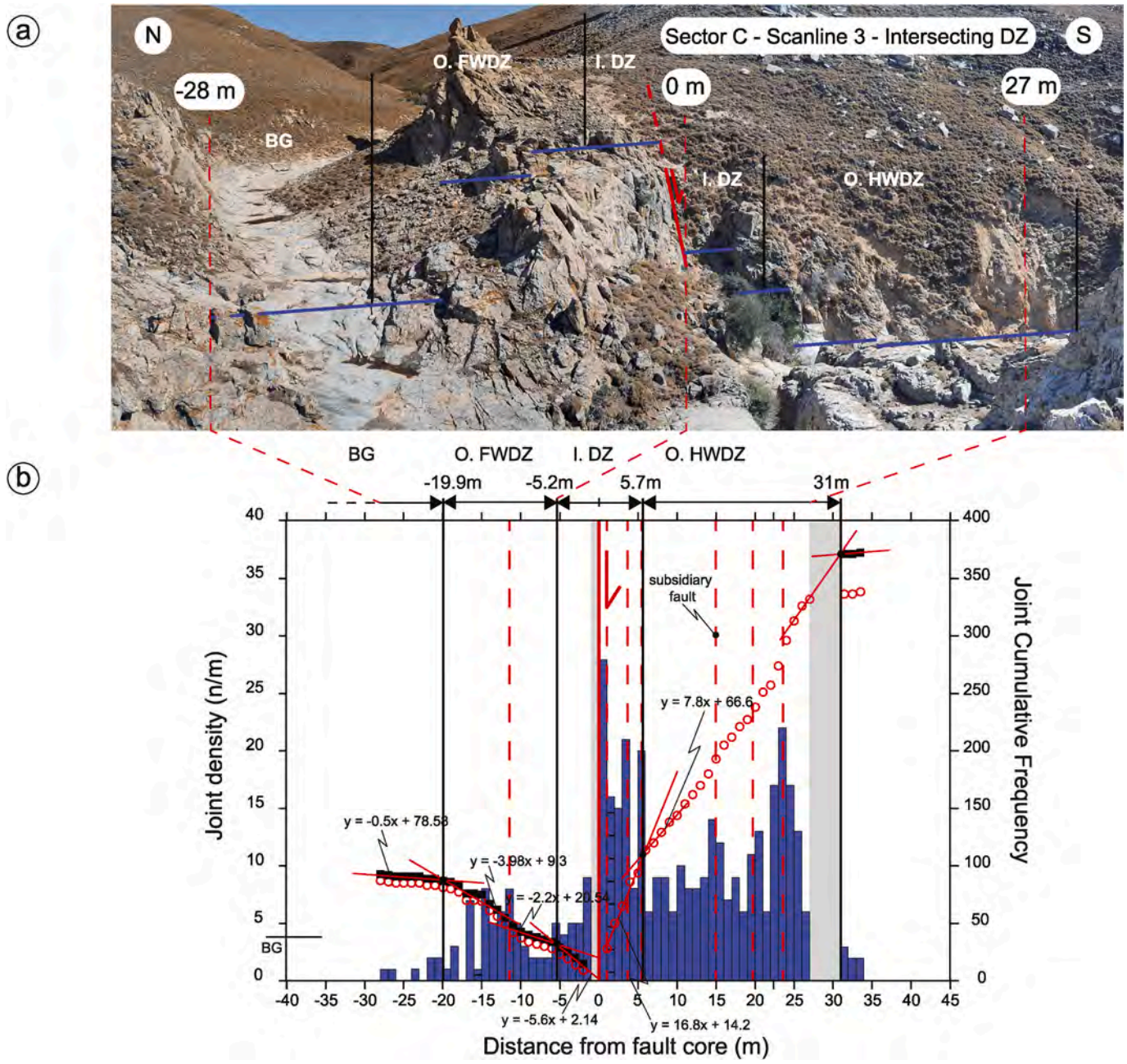


**Fig. 11.** (a) Photograph of the outcrop at structural site C4 showing the scan line traces that cross the intersecting damage zone of sector C (SC2). Acronyms as in previous figures. (b) Joint density vs distance from fault core plot. Normal frequency as bar diagrams, cumulative frequency as red empty dots (original data) and black squares (corrected data). Dashed red lines are subsidiary normal faults. The colours of the bars indicate different lithologies (see the legend of previous figure for details). Acronyms as in previous figure. (For interpretation of the references to colour in this figure legend, the reader is referred to the Web version of this article.)

triangle than wall damage zones (Fig. 12e). In terms of fracture network connectivity, intersecting and tip damage zones have similar average $C_B$ values (1.53 and 1.60, respectively), but these values are significantly higher than the average $C_B$ value for wall damage zones (0.88; Fig. 12d).

## 5. Discussion

### 5.1. Joint density and joint density decay in damage zones

Outstanding exposures allowed us to produce an accurate analysis of the attitude of the subsidiary fractures, damage zone width, fracture density variations across the fault, fracture topology in three different structural positions including (i) the wall damage zone in the central portion of NW-trending fault segments, (ii) the tip damage zone at the western termination of the northern segment, and (iii) the intersecting damage zone where the NW-trending segment connects with the E-W segment (Figs. 3 and 4).

In the studied fault damage zones, joint density is higher than background levels, as commonly reported in studies of fault-related fracturing from the outcrop-to the km-scale (Figs. 13 and 15) (Walsh and Watterson, 1988; Choi et al., 2016; Balsamo et al., 2019; Lucca et al., 2020; Martinelli et al., 2020; Torabi et al., 2020). Moreover, in the wall and intersecting damage zones deformation density decreases with increasing distance from the fault core (Figs. 13 and 14a) (Shipton and Cowie, 2001, 2003; Mitchell and Faulkner, 2009; Faulkner et al., 2010; Savage and Brodsky, 2011; Choi et al., 2016; Mayolle et al., 2019;

**Table 2**
Summary of topological analysis in wall, tip and intersecting damage zones including node and branch types and their proportions. <D> average degree; $C_B$ connections per branch. See text for definition. FWDZ, footwall damage zone; HWDZ hanging wall damage zone. Scan area IDs are referred to Fig. 12.

| Scan area ID | Damage zone type | Distance from fault core (m) | Nodes | | | Node proportions (%) | | | Branches | | | Branch proportions (%) | | | Degree of connectivity | |
|---|---|---|---|---|---|---|---|---|---|---|---|---|---|---|---|---|
| | | | I | X | Y | $P_I$ | $P_X$ | $P_Y$ | CC | CI | II | $P_{CC}$ | $P_{CI}$ | $P_{II}$ | <D> | $C_B$ |
| 1 | Wall damage zone (Outer FWDZ) | −8 | 29 | 0 | 3 | 90.63 | 0.00 | 9.38 | 2 | 4.5 | 12.5 | 10.53 | 23.68 | 65.79 | 1.19 | 0.47 |
| 2 | Wall damage zone (Inner FWDZ) | −2 | 39 | 2 | 12 | 73.58 | 3.77 | 22.64 | 10 | 19 | 12.5 | 24.10 | 45.78 | 30.12 | 1.57 | 1.06 |
| 3 | Wall damage zone (Inner HWDZ) | +10 | 67 | 3 | 40 | 60.91 | 2.73 | 36.36 | 43.5 | 45 | 11 | 43.72 | 45.23 | 11.06 | 1.81 | 1.33 |
| 4 | Wall damage zone (Outer HWDZ) | +32 | 18 | 0 | 3 | 85.71 | 0.00 | 14.29 | 3 | 3 | 7.5 | 22.22 | 22.22 | 55.56 | 1.29 | 0.67 |
| 5 | Tip damage zone (Outer FWDZ) | −52 | 168 | 81 | 269 | 32.43 | 15.64 | 51.93 | 478.5 | 144.5 | 13.5 | 75.18 | 22.70 | 2.12 | 2.46 | 1.74 |
| 6 | Tip damage zone (Outer FWDZ) | −25 | 45 | 14 | 16 | 60.00 | 18.67 | 21.33 | 32.5 | 33.5 | 8.5 | 43.62 | 44.97 | 11.41 | 1.99 | 1.40 |
| 7 | Tip damage zone (Inner FWDZ) | −3 | 324 | 137 | 269 | 44.38 | 18.77 | 36.85 | 527 | 292.5 | 20 | 62.78 | 34.84 | 2.38 | 2.30 | 1.61 |
| 8 | Tip damage zone (Outer HWDZ) | +15 | 160 | 44 | 172 | 42.55 | 11.70 | 45.74 | 282.5 | 126.5 | 18 | 75.13 | 29.63 | 4.22 | 2.27 | 1.62 |
| 9 | Tip damage zone (Outer HWDZ) | +35 | 66 | 24 | 63 | 43.14 | 15.69 | 41.18 | 116 | 53 | 6.5 | 75.82 | 30.20 | 3.70 | 2.29 | 1.62 |
| 10 | Intersecting damage zone (Inner FWDZ) | −3 | 19 | 5 | 47 | 26.76 | 7.04 | 66.20 | 66.5 | 22.5 | 1 | 93.66 | 25.00 | 1.11 | 2.54 | 1.79 |
| 11 | Intersecting damage zone (Inner HWDZ) | +2 | 38 | 13 | 52 | 36.89 | 12.62 | 50.49 | 81.5 | 37 | 4.5 | 79.13 | 30.08 | 3.66 | 2.39 | 1.69 |
| 12 | Intersecting damage zone (Outer HWDZ) | +8 | 60 | 17 | 51 | 46.88 | 13.28 | 39.84 | 85.5 | 43.5 | 11.5 | 66.80 | 30.96 | 8.19 | 2.20 | 1.57 |
| 13 | Intersecting damage zone (Outer HWDZ) | +15 | 28 | 4 | 5 | 75.68 | 10.81 | 13.51 | 8.5 | 15 | 6 | 22.97 | 50.85 | 20.34 | 1.59 | 1.05 |

Ceccato et al., 2021). In the wall and intersecting damage zones, the numbers of lithons bounded by fractures decreases with increasing distance from the fault core whereas their size increases (Sanderson et al., 2019). However, joint density data exhibit a high variability in the studied exposures (Figs. 9–11), even when moving average analysis is used (Fig. 13). Among the three cases, higher variability occurs in tip and intersecting damage zones (Fig. 13). A straightforward reason to explain this feature is the positive correlation between higher density values and presence of subsidiary faults (Fig. 13), which produced additional jointing adjacent to them. This inference is supported by the lower amplitude variability of the moving average curve of the wall damage zone, where subsidiary faults are less widespread (Fig. 13).

Power-law functions best fit the decreasing trend observed in the intersecting damage zone and in the footwall wall damage zone (Fig. 14a) (Savage and Brodsky, 2011; Ostermeijer et al., 2020; Ceccato et al., 2021). Data variability is responsible for the low correlation coefficients (R) of power-law best fits (Fig. 14a). However, in footwall wall and intersecting damage zones, R values are still in the range of those reported by Savage and Brodsky (2011). The power law slope coefficient (n) varies between −0.41 and −0.53 and falls within the range of values expected for fault zones accommodating displacement greater than 150 m (Savage and Brodsky, 2011). The rates of decay are relatively low compared to other fault zones having displacement of the same order of magnitude and similar faulted lithologies (sandstones) such as the Bartlett Fault (Moab Fault; Torabi et al., 2020), for which frequency data exhibit an abrupt decrease with increasing distance from the master slip surface. It must be emphasised, however, that sandstone silicification along the KAIF prevents a detailed comparison with other fault zones in sandstones.

In the tip damage zone, deformation density does not decrease towards background levels in the documented SC2 cross-section, even after the smoothing of local fluctuations related to subsidiary faults (Figs. 13b and 14a). This evidence is somehow expected in a peculiar sector of the fault zone that, by definition, is characterized by rapid along-strike displacement decrease, which is dissipated by the significant contribution of deformation spreading over larger areas (e.g., Perrin et al., 2016), as indicated by data in SC2 that, despite its length, did not reach damage zone boundaries on both footwall and hanging wall sides (Fig. 13b).

Total damage zone widths range between 50.9 and more than 122 m and fall within the range of those associated with faults having hundreds of meters displacements (Fig. 14b; e.g., Beach et al., 1999; Mitchell and Faulkner, 2009; Balsamo et al., 2016, 2019; Mayolle et al., 2019; Ma et al., 2023). Analysis of cumulative distributions on the frequency plots allows us to identify outer and an inner damage zones, based on joint density (Figs. 9–11; e.g., Berg and Skar, 2005; Torabi et al., 2020). In all studied sectors, the width of the inner damage zones does not vary much and is not proportional to the total damage zone width (Figs. 9–11, Table 1). Both in the inner and in the outer subdomains, mean joint densities are in some cases higher than those of other extensional fault zones described in the literature, deforming volcanic and/or siliciclastic rocks and having displacement similar to the KAIF (Bartlett Fault, Torabi et al., 2020; Pajarito Fault, Riley et al., 2010). In other cases, documented fracture densities are in the same range of what reported for other extensional fault zones in siliciclastic rocks, such as the four cross-sections of the Moab Fault proposed in Berg and Skar (2005). This large spread of deformation intensity among different outcrop studies from the literature is due to several factors including depth of deformation, inherited mechanical anisotropies, rock petrophysical properties at the time of deformation, type of deformation structures (e.g., deformation bands versus fractures), and mechanical stratigraphy. In the case of the KAIF, the along-strike partitioning of displacement can not be strongly constrained by the lack of robust correlation markers, whereas the occurrence of locally very intense silicification dramatically changed the rheological properties of the rocks and, consequently, their mechanical behaviour at the time of deformation.

### 5.2. *Tip versus wall damage zones: evidence for constant length fault growth*

Along the KAIF, both localized (i.e., wall damage zone) and distributed (i.e., tip damage zone) deformation coexist at different

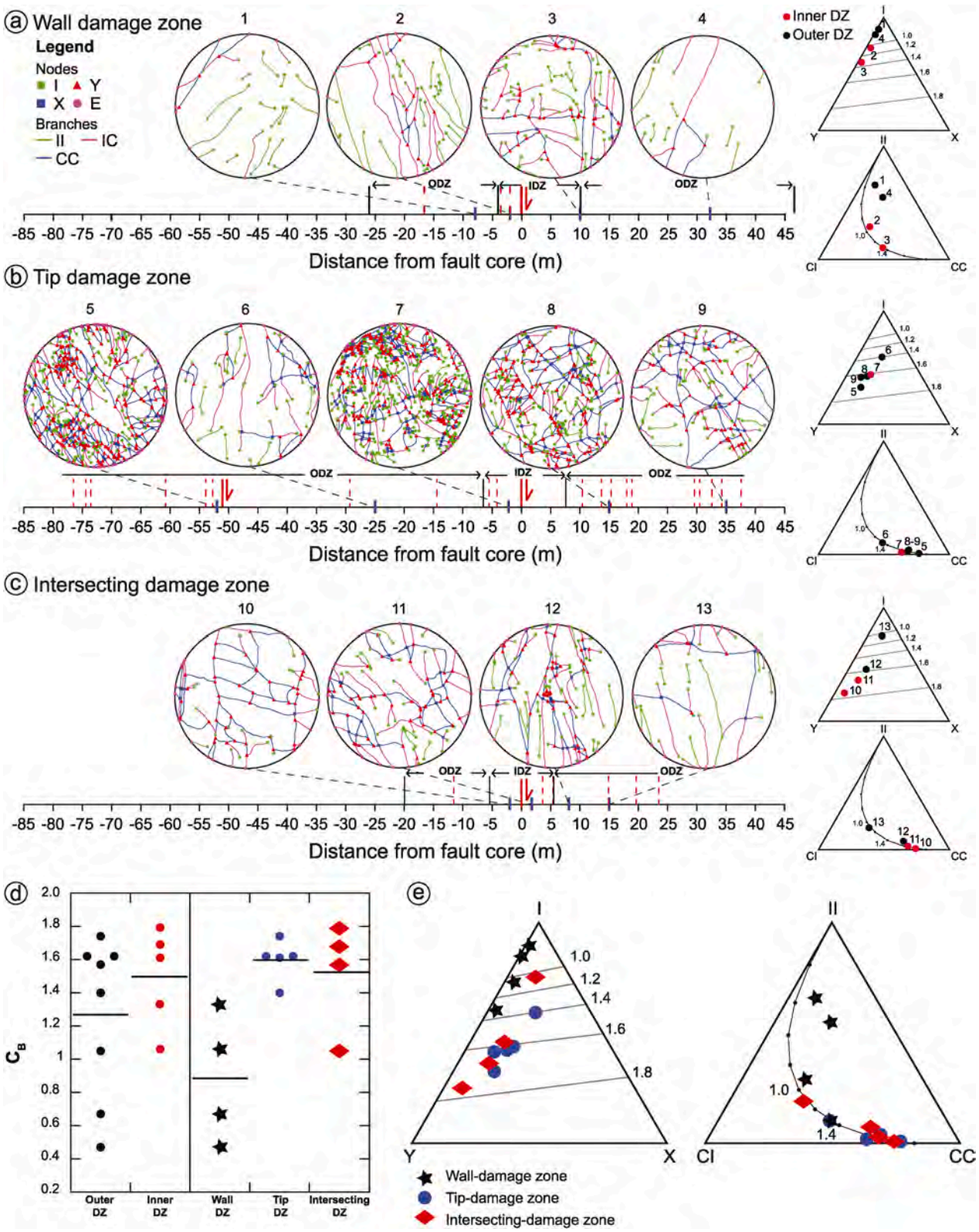


**Fig. 12.** (a–c) Digitized fracture networks in circular scan areas (diameter 1 m) illustrating the different node and branch types in each damage zone type. Scan areas are located along across-fault transects and their location with respect to the fault core is indicated below with blue marks. Dashed red lines represent subsidiary faults. Node and branch triangles (right) illustrating the proportion of I, X and Y nodes and those of II-, CI- and CC-branches in each damage zone type, respectively. Wall damage zone is presented in (a). Tip damage zone is presented in (b). Intersecting damage zone is presented in (c). (d) Dot plot showing the variability of the *connections per branch* ($C_B$) parameter in the outer and inner damage zone subdomains and in wall, tip and intersecting damage zones. The black lines represent average values. (e) Cumulative node and branch triangles (right) illustrating how the proportion of I, X and Y nodes and those of II-, CI- and CC-branches vary in the three different damage zone types. (For interpretation of the references to colour in this figure legend, the reader is referred to the Web version of this article.)

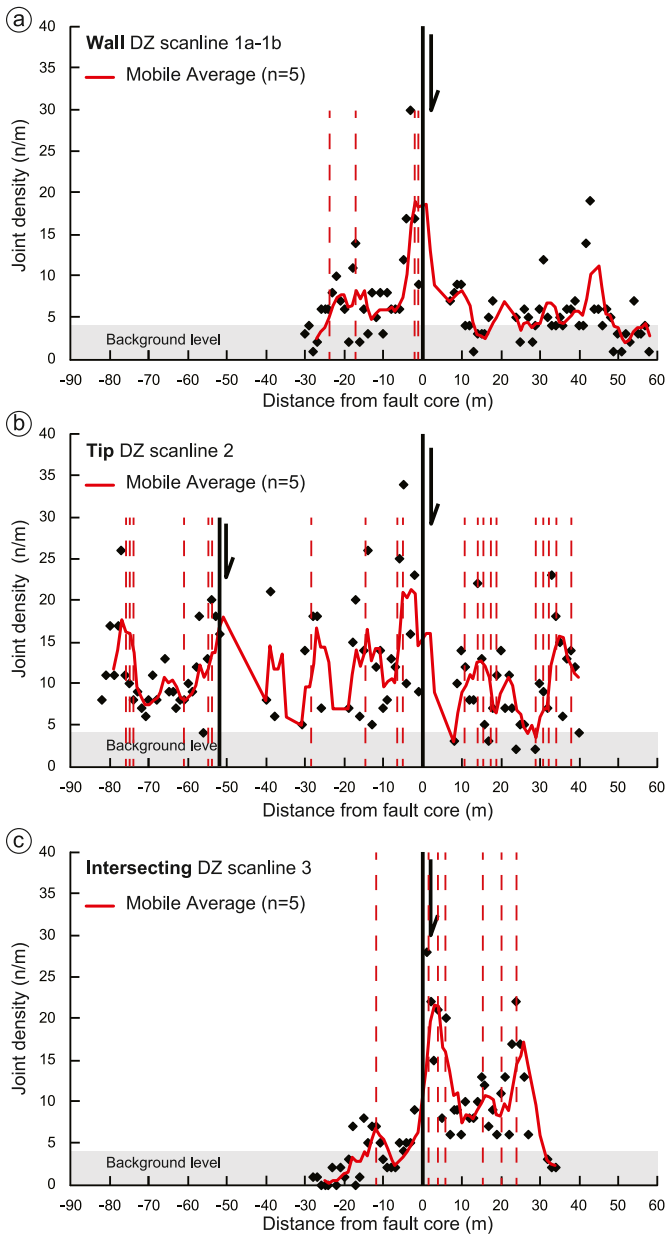


**Fig. 13.** Aligned scanline datasets (fracture frequency vs distance from fault core) for the three damage zone types. Black lines are master faults and dashed red lines are subsidiary faults. Light grey boxes are the mean background fracture frequency. The red lines are the moving average curves calculated by progressively averaging n = 5 data. (a) Wall damage zones of sector B and D. (b) Tip damage zone of sector A. (c) Intersecting damage zone of sector C. (For interpretation of the references to colour in this figure legend, the reader is referred to the Web version of this article.)

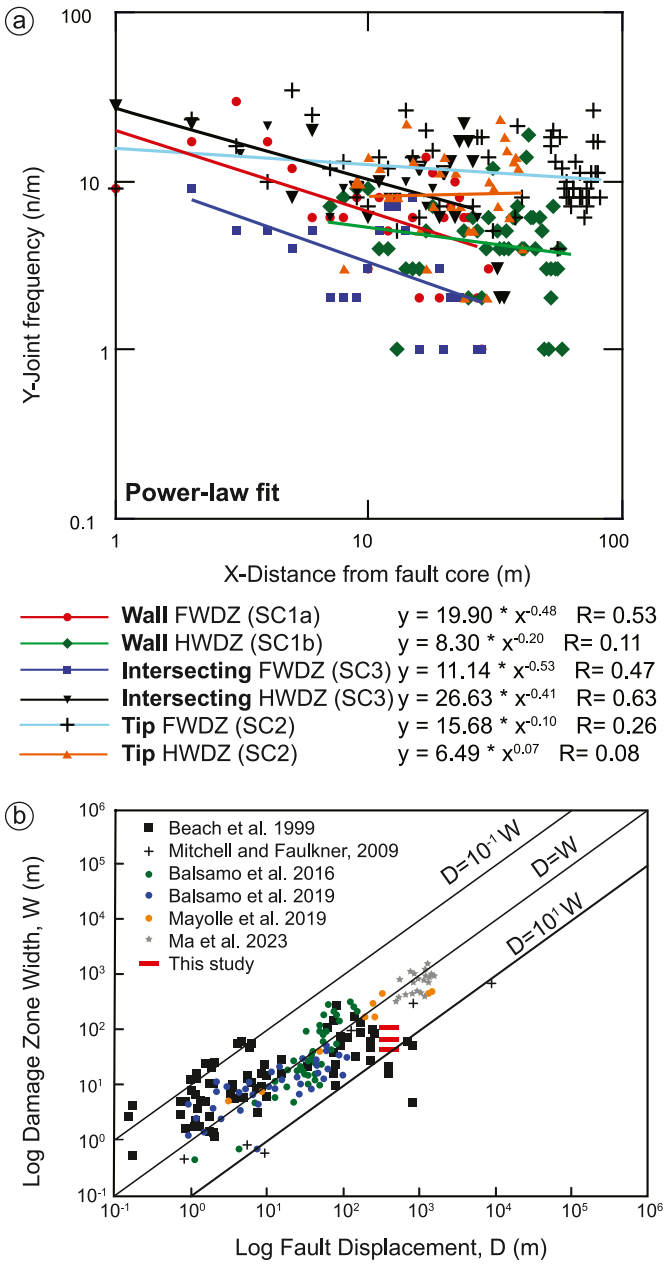


**Fig. 14.** (a) Scatter plot showing the variation in fracture frequency with increasing distance from the fault core in the three damage zone types both in the hanging wall and in the footwall. Lines are power-law fits to each damage zone type (see the legend for details). R, correlation coefficient of the power-law fit. (b) Damage zone width versus fault displacement (W-D relationships) in log-log space. Data from this study (red bars) are compared to data from published literature. The displacement assumed is the maximum displacement inferred for the KAIF (300–500 m). Along-strike variations of displacement along the KAIF have not been considered here. (For interpretation of the references to colour in this figure legend, the reader is referred to the Web version of this article.)

positions along-strike, which is a common feature of many fault zones at different scales (e.g., Soliva and Schultz, 2008; Nixon et al., 2014). In particular, the tip damage zone of the KAIF differs from wall damage zones by: (i) a greater damage zone width (Figs. 9 and 10, 13a-b, 15, Table 1); (ii) a higher joint density both in the inner and outer damage zones (Figs. 9, 10b and 13a-b, Table 1); (iii) a more distributed deformation consisting of tens of subsidiary faults (Figs. 9, 10b and 13a-b, 15); (iv) damage structures less systematically oriented (Figs. 7b–e, 15); and (v) a higher fracture connectivity that does not substantially change between inner and outer subdomains (Figs. 12 and 15, Table 2). Accordingly, our data indicate that the tip damage zone of the KAIF has peculiar characteristics, which are not documented elsewhere along the fault system. This evidence does not support the hypothesis that wall damage zones derived from tip damage zones that were progressively abandoned during fault lengthening as the tip propagated farther away along-strike (e.g., Kim et al., 2004), synchronously with fault slip (i.e. "propagating" or "increasing length" fault growth model; Nicol et al., 2017; Rotevatn et al., 2018). Conversely, the structural architecture of the KAIF suggests that the fault termination sector reasonably remained stationary after an initial phase of fault lengthening (i.e. "constant

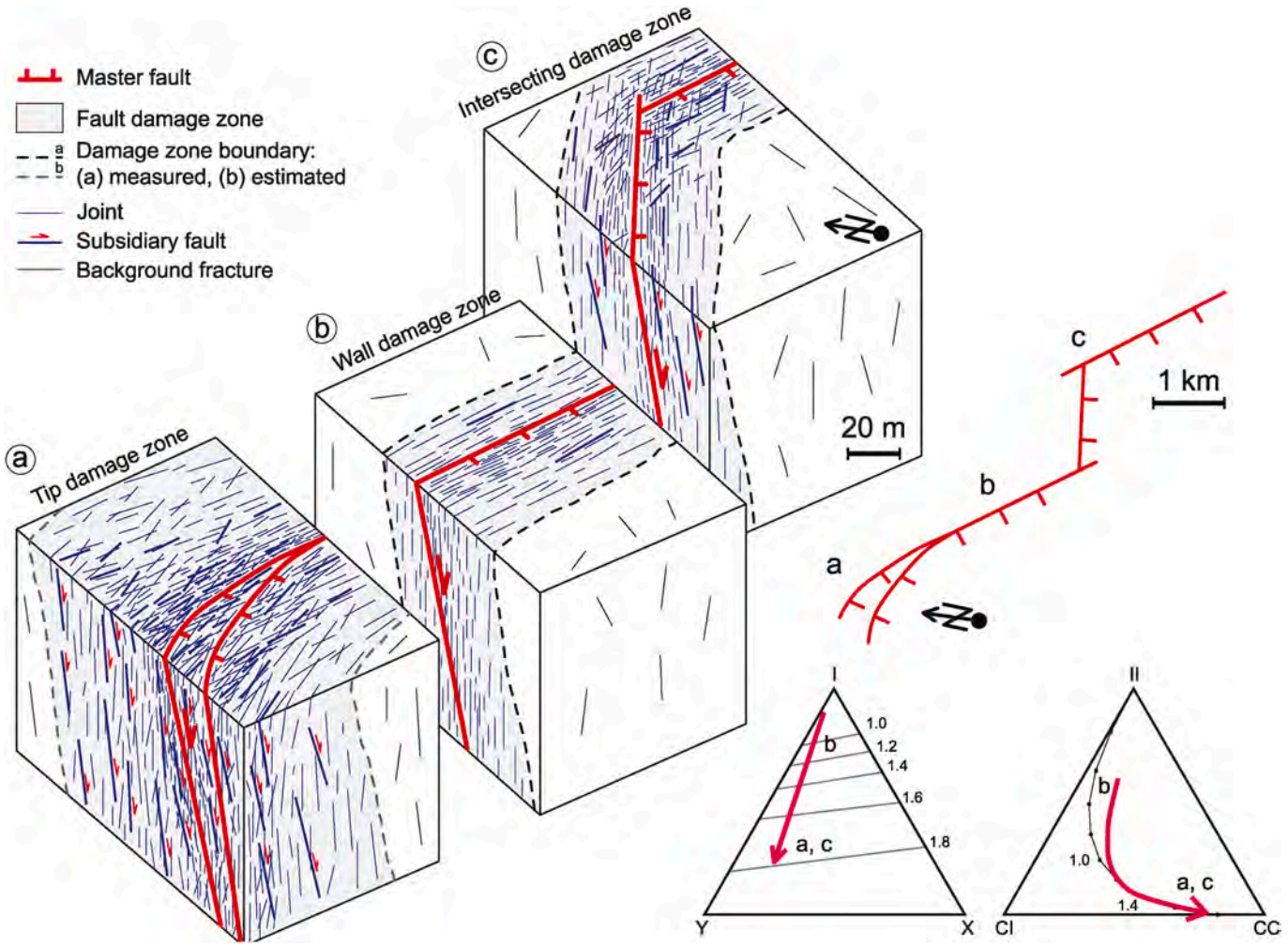


**Fig. 15.** Conceptual model showing the variation of damage zone parameters within tip damage zone (a), wall damage zone (b) and intersecting damage zone (c). The 3D blocks and the schematic sketches have different scales. Node and branch triangles (right) schematically illustrate the variation in fracture connectivity in the three damage zone types. See text for details.

length" fault growth model; Rotevatn et al., 2018).

In the tip damage zones, despite displacement tapers to zero (e.g., Manighetti et al., 2004; Balsamo et al., 2016), damage zone width is higher than elsewhere along fault strike, thus supporting the notion that, other than depending on finite displacement (e.g., Torabi and Berg, 2011; Choi et al., 2016; Torabi et al., 2020), fault zone thickness is a function of the structural position (e.g., Evans, 1990; Davatzes et al., 2005; Fondriest et al., 2015). A high fracture density in tip damage zones (e.g. Vermilye and Scholz, 1999; Davatzes et al., 2005; Nicol et al., 2017) can be due to stress concentrations, especially tensile stress, in the rock volume enclosing the tip (Cowie and Scholz, 1992; Davatzes et al., 2005; Perrin et al., 2016). The excess on-fault stress that results from the gradual decrease of fault displacement is distributed into the host rock off the fault, where it produces additional fracturing (Vermilye and Scholz, 1999; Perrin et al., 2016), and subsidiary faults with associated damage zones in horsetail arrays, which increase the local (metre scale) fracture density (e.g., Ostermeijer et al., 2020; Torabi et al., 2020). Since the place of measurement substantially impact on damage zone width, scaling relationships between fault displacement and damage-zone width should be cautiously applied, particularly when the 2D and 3D architecture of a fault system is poorly constrained (e.g., Evans, 1990; Davatzes et al., 2005; Quevedo et al., 2023).

### 5.3. Intersecting versus wall damage zones

Fault linkage is a common process during the growth of fault systems (e.g., Childs et al., 1995; Acocella et al., 2000; Hodge et al., 2018). In the KAIF, the E-W segment (sector C) likely developed by breaching the relay zone between the two NW-trending segments (sector B and D; Fig. 3), possibly in the late evolutionary history of the fault system. Hence, sector C likely accommodated a lower cumulative displacement than the other NW-SE striking segments (e.g., Childs et al., 1995; Hodge et al., 2018). Keeping in mind this consideration, our results show important differences in the intersecting damage zones when compared with wall damage zones (Figs. 13 and 15). In the former, strain is typically more distributed than in wall damage zones, with several subsidiary faults accommodating offsets and carrying their own damage structures (e.g., Nixon et al., 2019). In the intersecting damage zone of the KAIF, subsidiary faults are particularly abundant in the hanging wall (Figs. 13c and 15). Moreover, compared to tip and wall damage zones, the intersecting damage zone is characterized by higher joint densities in the hanging wall than in the footwall and the hanging wall damage zone is slightly wider than the footwall one (Figs. 11b and 13c, Table 1). This feature agrees with the asymmetric deformation patterns observed elsewhere between hanging wall and footwall blocks of inclined faults (e.g., Mitra and Ismat, 2001; Berg and Skar, 2005; Riley et al., 2010; Balsamo et al., 2019; Smeraglia et al., 2021). A possible explanation for the wider and more deformed hanging wall damage zone is the

asymmetric stress field that develops during extensional fault slip (e.g., Berg and Skar, 2005; Riley et al., 2010).

In the KAIF intersecting damage zone, deformation structures are less systematically oriented than in the wall damage zones (Figs. 7b–e, 15, Table 1). The standard deviation of joints and faults azimuthal data is slightly higher than the corresponding one in the tip damage zone (Table 1). Our structural data point out that, in the proximity of the connection point between the breaching E-W segment and the NW-SE one, deformation structures are parallel to either the E-W- or to the NW-SE fault segment (Figs. 7d and 15), thus creating a high structural complexity with a wider range of fracture orientation. This feature is commonly found in both soft- and hard-linked relay zones (e.g., Rotevatn and Bastesen, 2014).

### 5.4. Across- and along-fault variations in fracture connectivity: implications for permeability

Topological data presented in this work indicate a higher fracture connectivity in the inner damage zones than in the outer ones in sector B-D (wall damage zones) and in sector C (intersecting damage zone) (Fig. 12d–e). This is in agreement with topological analyses elsewhere that show an increase in connecting nodes approaching fault cores (Lucca et al., 2020; Hansberry et al., 2021). Data collected across the KAIF show that the increase in connectivity occurs both in the hanging wall and in the footwall. Hence, hanging wall and footwall rock volumes characterized by a high fracture connectivity and related high permeability are separated by a low permeability fault core made up of cohesive breccia and cataclasite (silicified) and by discrete master slip surfaces that are known to represent efficient across-fault barrier to flow (e.g., Curzi et al., 2023b). Published topological datasets document a general gradual decrease in connectivity over a distance of hundreds of meters from the fault core (Lucca et al., 2020; Hansberry et al., 2021). Topological data of the KAIF constrain a sharp drop in fracture connectivity over a short distance from the fault core, almost equal or only slightly wider than the inner damage zone (in the range of 5–20 m from the fault core), which is the only fault zone sector with a high proportion of connecting nodes and $C_B$ values over 1.5 (Fig. 12a, c).

Our results also show that this across-fault trend in fracture connectivity is not verified in the tip damage zone, where fracture connectivity remains high through the entire damage zone width. This feature can be due to a combination of (i) a persistently high fracture density with greater probability that fractures intersect (Fig. 13b), (ii) a larger proportion of subsidiary extensional faults that have a favourable dip angle to promote the formation of connecting X and Y nodes and (iii) a higher standard deviation of deformation structure strike. The larger azimuthal variability in tip damage zones can be the result of the altered state of stress in the proximity of the fault tip (e.g. Vermilye and Scholz, 1999). This may have a fundamental impact on the fracture network connectivity and hence on fluid flow since it implies a greater probability that fractures intersect and remain open in any given stress field (e.g., Sanderson and Nixon, 2018). The average $C_B$ value for the KAIF tip damage zone (1.60) is in accordance with those of complex tip damage zones (horsetail and bifurcating tips) shown in Nixon et al. (2020) for carbonate-hosted extensional fault zones with much smaller displacements. The bleaching pattern of sandstones observed in the footwall tip damage zone of the KAIF may testify the highly connected paleo-fluid paths that allowed iron mobilization (e.g., Parry et al., 2004; Torabi et al., 2020).

Topological data in the intersecting damage zone show a higher proportion of connecting nodes and of partially/fully connected branches, thus substantially higher $C_B$ values (Fig. 12 d-e, Table 2), likely due to the presence of two sets of deformation structures, which strongly enhances fracture connectivity in the structurally complex linkage sector. The mean $C_B$ value for the intersecting damage zone (1.53) is almost equal to that of tip damage zone and is in the range typical for damage zones near geometrically or kinematically linked extensional faults ($C_B$ = 1.2–1.9) as shown by (Fig. 12e) Nixon et al. (2020; Table 2). These results confirm that both soft and hard linkage processes can affect damage zone parameters (e.g., Kim and Sanderson, 2005; Person et al., 2012; Alaei and Torabi, 2017; Walter et al., 2019; Mercuri et al., 2020; Torabi et al., 2021). Accordingly, fault intersections and fault oversteps can represent areas of enhanced secondary permeability that have to be taken into consideration (Kim and Sanderson, 2010; Person et al., 2012; Balsamo et al., 2016; Peacock et al., 2017) since they possibly compromise trap integrity representing potential leakage zones for geofluids (e.g. Gartrell et al., 2004).

## 6. Conclusions

The Kornos-Aghios Ioannis Fault (KAIF) is an extensional fault system which deformed at shallow depth (<1 km) Cenozoic turbidite sandstones and igneous rocks, with an inferred maximum dip-slip displacement of some hundreds of meters. In this work, we described the 2D fault geometry and kinematics as well as the fault damage zone parameters. Outstanding exposures allowed us to produce an accurate analysis of the attitude of the subsidiary fractures, damage zone width, joint density variations across the fault, and fracture topology, in three different structural positions including (i) the wall damage zone in the central portion of NW-trending fault segments, (ii) the tip damage zone at the western termination of the northern segment, and (iii) the intersecting damage zone where the NW-trending segments are connected by the E-W segment. The following conclusive major points can be drawn from our results.

- The width of the tip damage zone (>122 m) is much greater than that of the wall and intersecting damage zones (50.9 and 72.6m, respectively).
- The tip damage zone is characterized by higher joint density compared to the wall and intersecting damage zones. This additional fracturing includes subsidiary faults that have their own damage structures causing several fluctuations in joint density.
- Joints in the tip and intersecting damage zones are less systematically oriented compared to the wall damage zones. Accordingly, our topological data attest that tip and intersecting damage zones are characterized by higher fracture connectivity compared to wall damage zones.
- In wall and intersecting damage zones, fracture connectivity varies across-fault and particularly it abruptly increases approaching the fault. In the tip damage zone, fracture connectivity remains high through the entire damage zone width.

This work indicates that the structural architecture of the extensional fault system controls damage zone parameters and that fault intersections and tip regions can represent areas of enhanced secondary permeability and, hence, potential leakage zones for geofluids. The structural variability along-strike may contribute to explain the large scattering of displacement-damage zone thickness datasets. Accordingly, displacement-thickness correlations should be cautiously applied, particularly if the 2D and 3D architecture of the fault system is poorly known. This study shows the high complexity of damage zone parameters associated with an extensional fault system and testifies that models of faulted/fractured rock volumes can be even more refined through detailed and extensive field-based constraints.

## CRediT authorship contribution statement

**L.R. Berio:** Conceptualization, Data curation, Formal analysis, Investigation, Methodology, Validation, Roles, Writing – original draft, Writing – review & editing. **F. Balsamo:** Conceptualization, Formal analysis, Investigation, Methodology, Validation, Roles, Writing – original draft, Writing – review & editing, Funding acquisition, Project administration. **M. Pizzati:** Investigation, Methodology, Validation,

Roles, Writing – original draft, Writing – review & editing. **F. Storti:** Investigation, Methodology, Validation, Roles, Writing – original draft, Writing – review & editing. **M. Curzi:** Investigation, Methodology, Validation, Roles, Writing – original draft, Writing – review & editing. **G. Viola:** Investigation, Methodology, Validation, Roles, Writing – original draft, Writing – review & editing, Funding acquisition, Project administration.

## Declaration of competing interest

The authors declare the following financial interests/personal relationships which may be considered as potential competing interests: Giulio Viola reports financial support was provided by Italian Ministry of University, and Research (MUR).

## Data availability

I have shared the link to my data in the manuscript file. All the data used in this paper are available at https://data.mendeley.com/datasets/3rr4926xp5/1.

## Acknowledgments

We are extremely grateful to David Sanderson and an anonymous reviewer for their constructive comments that significantly improved the manuscript. The Editor Fabrizio Agosta is thanked for the precise editorial work. We acknowledge financial support by the Italian Ministry of University, and Research (MUR) through PRIN project "FAST-Fault architecture in space and time" (PRIN 2020, PI G. Viola, local coordinator F. Balsamo; CUP J33C22000170001). This work has benefited from the equipment and framework of the "COMP-HUB" and "COMP-R" Initiatives, funded by the "Departments of Excellence" program of the Italian Ministry for University and Research (MIUR, 2018–2022 and MUR, 2023–2027).

## References

Acocella, V., Gudmundsson, A., Funiciello, R., 2000. Interaction and linkage of extension fractures and normal faults: examples from the rift zone of Iceland Valerio. J. Struct. Geol. 22, 1233–1246. https://doi.org/10.1016/S0191-8141(00)00031-6.

Agosta, F., 2008. Fluid Flow Properties of Basin-Bounding Normal Faults in Platform Carbonates, Fucino Basin, Central Italy, vol. 299. Geological Society Special Publication, pp. 277–291. https://doi.org/10.1144/SP299.17.

Alaei, B., Torabi, A., 2017. Seismic imaging of fault damaged zone and its scaling relation with displacement. Interpretation 5, SP83–SP93. https://doi.org/10.1190/int-2016-0230.1.

Anifadi, A., Parcharidis, I., Sykioti, O., 2017. Hydrothermal alteration zones detection in Limnos Island, through the application of remote sensing. Bull. Geol. Soc. Greece 50, 1595–1604. https://doi.org/10.12681/bgsg.11879.

Armijo, R., Meyer, B., Hubert, A., Barka, A., 1999. Westward propagation of the North Anatolian Fault into the northern Aegean: timing and kinematics. Geology 27, 267–270. https://doi.org/10.1130/0091-7613(1999)027<0267:WPOTNA>2.3.CO;2.

Aubert, I., Léonide, P., Lamarche, J., Salardon, R., 2019. Diagenetic evolution of fault zones in Urgonian microporous carbonates, impact on reservoir properties (Provence – SE France). Solid Earth 11, 1163–1186. https://doi.org/10.5194/se-11-1163-2020.

Aydin, A., 2000. Fractures, faults, and hydrocarbon entrapment, migration and flow. Mar. Petrol. Geol. 17, 797–814. https://doi.org/10.1016/S0264-8172(00)00020-9.

Balsamo, F., Clemenzi, L., Storti, F., Mozafari, M., Solum, J., Swennen, R., Taberner, C., Tueckmantel, C., 2016. Anatomy and paleofluid evolution of laterally restricted extensional fault zones in the Jabal Qusaybah anticline, Salakh Arch, Oman. Bull. Geol. Soc. Am. 128, 957–972. https://doi.org/10.1130/B31317.1.

Balsamo, F., Clemenzi, L., Storti, F., Solum, J., Taberner, C., 2019. Tectonic control on vein attributes and deformation intensity in fault damage zones affecting Natih platform carbonates, Jabal Qusaybah, North Oman. J. Struct. Geol. 122, 38–57. https://doi.org/10.1016/j.jsg.2019.02.009.

Beach, A., Welbon, A.I., Brockbank, P.J., McCallum, J.E., 1999. Reservoir damage around faults: outcrop examples from the Suez rift. Petrol. Geosci. 5, 109–116. https://doi.org/10.1144/petgeo.5.2.109.

Berg, S.S., Skar, T., 2005. Controls on damage zone asymmetry of a normal fault zone: outcrop analyses of a segment of the Moab fault, SE Utah. J. Struct. Geol. 27, 1803–1822. https://doi.org/10.1016/j.jsg.2005.04.012.

Bonev, N., Beccaletto, L., 2007. In: Taymaz, T., Yilmaz, Y., Dilek, Y. (Eds.), The Geodynamics of the Aegean and Anatolia, 291. Geological Society Special Publication, pp. 113–142. https://doi.org/10.1144/SP291.6.

Busch, A., Kampman, N., 2018. Migration and leakage of CO2 from deep geological storage sites. In: Vialle, S., Ajo-Franklin, J., Carey, J.W. (Eds.), Geological Carbon Storage: Subsurface Seals and Caprock Integrity, Geophys. Monogr, 238, pp. 285–303. https://doi.org/10.1002/9781119118657.ch14.

Caine, J.S., Evans, J.P., Forster, C.B., 1996. Fault zone architecture and permeability structure. Geology 24, 1025–1028. https://doi.org/10.1130/0091-7613(1996)024<1025:FZAAPS>2.3.CO;2.

Caputo, R., Chatzipetros, A., Pavlides, S., Sboras, S., 2012. The Greek database of seismogenic sources (GreDaSS): state-of-the-art for northern Greece. Ann. Geophys. 55, 859–894. https://doi.org/10.4401/ag-5168.

Caracciolo, L., Critelli, S., Innocenti, F., Kolios, N., Manetti, P., 2011. Unravelling provenance from eocene-oligocene sandstones of the Thrace Basin, north-east Greece. Sedimentology 58, 1988–2011. https://doi.org/10.1111/j.1365-3091.2011.01248.x.

Ceccato, A., Viola, G., Antonellini, M., Tartaglia, G., Ryan, E.J., 2021. Constraints upon fault zone properties by combined structural analysis of virtual outcrop models and discrete fracture network modelling. J. Struct. Geol. 152, 104444 https://doi.org/10.1016/j.jsg.2021.104444.

Childs, C., Manzocchi, T., Walsh, J.J., Bonson, C.G., Nicol, A., Schöpfer, M.P.J., 2009. A geometric model of fault zone and fault rock thickness variations. J. Struct. Geol. 31, 117–127. https://doi.org/10.1016/j.jsg.2008.08.009.

Childs, C., Watterson, J., Walsh, J.J., 1995. Fault overlap zones within developing normal fault systems. J. Geol. Soc. 152, 535–549. https://doi.org/10.1144/gsjgs.152.3.0535.

Choi, J.H., Edwards, P., Ko, K., Kim, Y.S., 2016. Definition and classification of fault damage zones: a review and a new methodological approach. Earth Sci. Rev. 152, 70–87. https://doi.org/10.1016/j.earscirev.2015.11.006.

Congro, M., Zanatta, A., Oliveira, K., Quevedo, R., Carvalho, B.R., Roehl, D., 2023. In: Determination of Fault Damage Zones in Sandstone Rocks Using Numerical Models and Statistical Analyses, 36. Geomechanics for Energy and the Environment, 100495. https://doi.org/10.1016/j.gete.2023.100495.

Cowie, P.A., Scholz, C.H., 1992. Physical explanation for the displacement-length relationship of faults using a post-yield fracture mechanics model. J. Struct. Geol. 14, 1133–1148. https://doi.org/10.1016/0191-8141(92)90065-5.

Curzi, M., Cipriani, A., Aldega, L., Billi, A., Carminati, E., Van der Lelij, R., Vignaroli, G., Viola, G., 2023a. Architecture and permeability structure of the Sibillini Mts. Thrust and influence upon recent, extension-related seismicity in the central Apennines (Italy) through fault-valve behavior. Geol. Soc. Am. Bull. 1–24.

Curzi, M., Giuntoli, F., Vignaroli, G., Viola, G., 2023b. Constraints on upper crustal fluid circulation and seismogenesis from in-situ outcrop quantification of complex fault zone permeability. Sci. Rep. 13, 5548. https://doi.org/10.1038/s41598-023-32749-4.

Davatzes, N.C., Eichhubl, P., Aydin, A., 2005. Structural evolution of fault zones in sandstone by multiple deformation mechanisms: Moab fault, southeast Utah. Bull. Geol. Soc. Am. 117, 135–148. https://doi.org/10.1130/B25473.1.

Evans, J.P., 1990. Thickness-displacement relationship of fault zones. J. Struct. Geol. 12, 1061–1065. https://doi.org/10.1016/0191-8141(90)90101-4.

Faulkner, D.R., Jackson, C.A.L., Lunn, R.J., Schlische, R.W., Shipton, Z.K., Wibberley, C. A.J., Withjack, M.O., 2010. A review of recent developments concerning the structure, mechanics and fluid flow properties of fault zones. J. Struct. Geol. 32, 1557–1575. https://doi.org/10.1016/j.jsg.2010.06.009.

Ferrill, D.A., Morris, A.P., McGinnis, R.N., Smart, K.J., Wigginton, S.S., Hill, N.J., 2017. Mechanical stratigraphy and normal faulting. J. Struct. Geol. 94, 275–302. https://doi.org/10.1016/j.jsg.2016.11.010.

Fondriest, M., Aretusini, S., Di Toro, G., Smith, S.A.F., 2015. Fracturing and rock pulverization along an exhumed seismogenic fault zone in dolostones: the Foiana Fault Zone (Southern Alps, Italy). Tectonophysics 654, 56–74. https://doi.org/10.1016/j.tecto.2015.04.015.

Fornadel, A.P., Voudouris, P.C., Spry, P.G., Melfos, V., 2012. Mineralogical, stable isotope, and fluid inclusion studies of spatially related porphyry Cu and epithermal Au-Te mineralization, Fakos Peninsula, Limnos Island, Greece. Mineral. Petrol. 105, 85–111. https://doi.org/10.1007/s00710-012-0196-8.

Fossen, H., Rotevatn, A., 2016. Fault linkage and relay structures in extensional settings-A review. Earth Sci. Rev. 154, 14–28. https://doi.org/10.1016/j.earscirev.2015.11.014.

Gartrell, A., Zhang, Y., Lisk, M., Dewhurst, D., 2004. Fault intersections as critical hydrocarbon leakage zones: integrated field study and numerical modelling of an example from the Timor Sea, Australia. Mar. Petrol. Geol. 21, 1165–1179. https://doi.org/10.1016/j.marpetgeo.2004.08.001.

Hansberry, R.L., King, R.C., Holford, S.P., Hand, M., Debenham, N., 2021. How wide is a fault damage zone ? Using network topology to examine how fault-damage zones overprint regional fracture networks. J. Struct. Geol. 146, 104327 https://doi.org/10.1016/j.jsg.2021.104327.

Hodge, M., Fagereng, Biggs, J., 2018. The role of coseismic coulomb stress changes in shaping the hard link between normal fault segments. J. Geophys. Res. Solid Earth 123, 797–814. https://doi.org/10.1002/2017JB014927.

Innocenti, F., Manetti, P., Mazzuoli, R., Pertusati, P., Fytikas, M., Kolios, N., 1994. The geology and geodynamic significance of the island of Limnos, North Aegean sea, Greece. Neues Jahrbuch Für Geologie Und Paläontologie 11, 661–691. https://doi.org/10.1127/njgpm/1994/1994/661.

Innocenti, F., Manetti, P., Mazzuoli, R., Pertusati, P., Fytikas, M., Kolios, N., Vougioukalakis, G.E., Androulakakis, N., Critelli, S., Caracciolo, L., 2009. Geological

map (scale 1:50,000) of Limnos island (Greece) : explanatory notes. Acta Vulcanol. 21, 123–134. https://doi.org/10.1400/146017.
Jeanne, P., Guglielmi, Y., Cappa, F., 2013. Dissimilar properties within a carbonate-reservoir's small fault zone, and their impact on the pressurization and leakage associated with CO2 injection. J. Struct. Geol. 47, 25–35. https://doi.org/10.1016/j.jsg.2012.10.010.
Jolivet, L., Brun, J.-P., Gautier, P., Lallemant, S., Patriat, M., 1994. 3D-kinematics of extension in the Aegean region from the early Miocene to the Present, insights from the ductile crust. Bull. Soc. Geol. Fr. 165, 195–209.
Jolivet, L., Brun, J.P., 2010. Cenozoic geodynamic evolution of the Aegean. Int. J. Earth Sci. 99, 109–138. https://doi.org/10.1007/s00531-008-0366-4.
Jolivet, L., Faccenna, C., Huet, B., Labrousse, L., Le Pourhiet, L., Lacombe, O., Lecomte, E., Burov, E., Denèle, Y., Brun, J.P., Philippon, M., Paul, A., Salaün, G., Karabulut, H., Piromallo, C., Monié, P., Gueydan, F., Okay, A.I., Oberhänsli, R., Pourteau, A., Augier, R., Gadenne, L., Driussi, O., 2013. Aegean tectonics: strain localisation, slab tearing and trench retreat. Tectonophysics 597–598, 1–33. https://doi.org/10.1016/j.tecto.2012.06.011.
Jolivet, L., Menant, A., Clerc, C., Sternai, P., Bellahsen, N., Leroy, S., Pik, R., Stab, M., Faccenna, C., Gorini, C., 2018. Extensional crustal tectonics and crust-mantle coupling, a view from the geological record. Earth Sci. Rev. 185, 1187–1209. https://doi.org/10.1016/j.earscirev.2018.09.010.
Kim, Y.S., Peacock, D.C.P., Sanderson, D.J., 2004. Fault damage zones. J. Struct. Geol. 26, 503–517. https://doi.org/10.1016/j.jsg.2003.08.002.
Kim, Y.S., Sanderson, D.J., 2010. Inferred fluid flow through fault damage zones based on the observation of stalactites in carbonate caves. J. Struct. Geol. 32, 1305–1316. https://doi.org/10.1016/j.jsg.2009.04.017.
Kim, Y.S., Sanderson, D.J., 2005. The relationship between displacement and length of faults: a review. Earth Sci. Rev. 68, 317–334. https://doi.org/10.1016/j.earscirev.2004.06.003.
Kiratzi, A.A., Svigkas, N., 2013. A study of the 8 january 2013 Mw5.8 earthquake sequence (Lemnos island, East Aegean sea). Tectonophysics 608, 452–460. https://doi.org/10.1016/j.tecto.2013.09.002.
Kirkpatrick, J.D., Shipton, Z.K., Evans, J.P., Micklethwaite, S., Lim, S.J., McKillop, P., 2008. Strike-slip fault terminations at seismogenic depths: the structure and kinematics of the Glacier Lakes fault, Sierra Nevada United States. J. Geophys. Res. Solid Earth 113, 1–15. https://doi.org/10.1029/2007JB005311.
Koukouvelas, I.K., Aydin, A., 2002. Fault structure and related basins of the North Aegean Sea and its surroundings. Tectonics 21. https://doi.org/10.1029/2001TC901037, 10–17.
Lucca, A., Storti, F., Molli, G., 2020. Extensional fracture network attribute distribution in faulted thick sandstone strata: compione Fault, Northern Apennines, Italy. J. Struct. Geol. 131, 103954 https://doi.org/10.1016/j.jsg.2019.103954.
Lucca, A., Storti, F., Molli, G., Muchez, P., Schito, A., Artoni, A., Balsamo, F., Corrado, S., Mariani, E.S., 2018. Seismically enhanced hydrothermal plume advection through the process zone of the Compione extensional Fault, Northern Apennines, Italy. GSA Bulletin 131, 547–571. https://doi.org/10.1130/b32029.1.
Ma, S., Zeng, L., Tian, H., Shi, X., Wu, W., Yang, S., et al., 2023. Fault damage zone and its effect on deep shale gas: insights from 3D seismic interpretation in the southern Sichuan Basin, China. J. Struct. Geol. 170, 104848 https://doi.org/10.1016/j.jsg.2023.104848.
Manighetti, I., King, G., Sammis, C.G., 2004. The role of off-fault damage in the evolution of normal faults. Earth Planet Sci. Lett. 217, 399–408. https://doi.org/10.1016/S0012-821X(03)00601-0.
Maravelis, A.G., Pantopoulos, G., Tserolas, P., Zelilidis, A., 2015. Accretionary prism–forearc interactions as reflected in the sedimentary fill of southern Thrace Basin (Lemnos Island, NE Greece). Int. J. Earth Sci. 104, 1039–1060. https://doi.org/10.1007/s00531-014-1130-6.
Martinelli, M., Bistacchi, A., Mittempergher, S., Bonneau, F., Balsamo, F., Caumon, G., Meda, M., 2020. Damage zone characterization combining scan-line and scan-area analysis on a km-scale Digital Outcrop Model: the Qala Fault (Gozo). J. Struct. Geol. 140, 104144 https://doi.org/10.1016/j.jsg.2020.104144.
Mayolle, S., Soliva, R., Caniven, Y., Wibberley, C., Ballas, G., Milesi, G., Dominguez, S., 2019. Scaling of fault damage zones in carbonate rocks. J. Struct. Geol. 124, 35–50. https://doi.org/10.1016/j.jsg.2019.03.007.
McGrath, A.G., Davison, I., 1995. Damage zone geometry around fault tips. J. Struct. Geol. 17, 1011–1024. https://doi.org/10.1016/0191-8141(94)00116-H.
Mercuri, M., Carminati, E., Tartarello, M.C., Brandano, M., Mazzanti, P., Brunetti, A., McCaffrey, K.J.W., Collettini, C., 2020. Lithological and structural control on fracture frequency distribution within a carbonate-hosted relay ramp. J. Struct. Geol. 137, 104085 https://doi.org/10.1016/j.jsg.2020.104085.
Mitchell, T.M., Faulkner, D.R., 2009. The nature and origin of off-fault damage surrounding strike-slip fault zones with a wide range of displacements: a field study from the Atacama fault system, northern Chile. J. Struct. Geol. 31, 802–816. https://doi.org/10.1016/j.jsg.2009.05.002.
Mitra, G., Ismat, Z., 2001. Microfracturing associated with reactivated fault zones and shear zones : what can it tell us about deformation history. In: Holdsworth, R.E., Strachan, R.A., Magloughlin, J.F., Knipe, R.J. (Eds.), The Nature and Tectonic Significance of Fault Zone Weakening. Geological Society, London, pp. 113–140. https://doi.org/10.1144/GSL.SP.2001.186.01.08. Special Publications 186.
Mozafari, M., Swennen, R., Balsamo, F., Clemenzi, L., Storti, F., El Desouky, H., Vanhaecke, F., Tueckmantel, C., Solum, J., Taberner, C., 2015. Paleofluid evolution in fault-damage zones: evidence from fault-fold interaction events in the Jabal Qusaybah anticline (Adam foothills, North Oman). J. Sediment. Res. 85, 1525–1551. https://doi.org/10.2110/jsr.2015.95.
Mozafari, M., Swennen, R., Balsamo, F., El Desouky, H., Storti, F., Taberner, C., 2019. Fault-controlled dolomitization in the Montagna dei Fiori Anticline (Central Apennines, Italy): record of a dominantly pre-orogenic fluid migration. Solid Earth 10, 1355–1383. https://doi.org/10.5194/se-10-1355-2019.
Nicol, A., Childs, C., Walsh, J.J., Manzocchi, T., Schöpfer, M.P.J., 2017. In: Childs, C., Holdsworth, R.E., Jackson, C.A.-L., Manzocchi, T., Walsh, J.J., Yielding, G. (Eds.), The Geometry and Growth of Normal Faults.Geological, 439. Society Special Publication, pp. 23–39. https://doi.org/10.1144/SP439.9.
Nixon, C.W., Bull, J.M., Sanderson, D.J., 2014. Localized vs distributed deformation associated with the linkage history of an active normal fault, Whakatane Graben, New Zealand. J. Struct. Geol. 69, 266–280. https://doi.org/10.1016/j.jsg.2014.06.005.
Nixon, C.W., Nærland, K., Rotevatn, A., Dimmen, V., Sanderson, D.J., Kristensen, T.B., 2020. Connectivity and network development of carbonate-hosted fault damage zones from western Malta. J. Struct. Geol. 141, 104212 https://doi.org/10.1016/j.jsg.2020.104212.
Nixon, C.W., Vaagan, S., Sanderson, D.J., Gawthorpe, R.L., 2019. Spatial distribution of damage and strain within a normal fault relay at Kilve, U.K. J. Struct. Geol. 118, 194–209. https://doi.org/10.1016/j.jsg.2018.10.016.
Nyberg, B., Nixon, C.W., Sanderson, D.J., 2018. NetworkGT: a GIS tool for geometric and topological analysis of two-dimensional fracture networks. Geosphere 14, 1618–1634. https://doi.org/10.1130/GES01595.1.
O'Hara, A.P., Jacobi, R.D., Sheets, H.D., 2017. Predicting the width and average fracture frequency of damage zones using a partial least squares statistical analysis: implications for fault zone development. J. Struct. Geol. 98, 38–52. https://doi.org/10.1016/j.jsg.2017.03.008.
Ostermeijer, G.A., Mitchell, T.M., Aben, F.M., Dorsey, M.T., Browning, J., Rockwell, T.K., Fletcher, J.M., Ostermeijer, F., 2020. Damage zone heterogeneity on seismogenic faults in crystalline rock; a field study of the Borrego Fault, Baja California. J. Struct. Geol. 137, 104016 https://doi.org/10.1016/j.jsg.2020.104016.
Papoulis, D., Tsolis-Katagas, P., 2008. Formation of alteration zones and kaolin genesis, Limnos Island, northeast Aegean Sea, Greece. Clay Miner. 43, 631–646. https://doi.org/10.1180/claymin.2008.043.4.08.
Parry, W.T., Chan, M.A., Beitler, B., 2004. Chemical bleaching indicates episodes of fluid flow in deformation bands in sandstone. AAPG (Am. Assoc. Pet. Geol.) Bull. 88, 175–191. https://doi.org/10.1306/09090303034.
Pavlides, S., Mountrakis, D., Kilias, A., Tranos, M., 1990. The role of strike-slip movements in the extensional area of Northern Aegean (Greece). A case of transtensional tectonics. Ann. Tect. 4, 196–211.
Pavlides, S., Tranos, M.D., 1991. Structural characteristics of two strong earthquakes in the North Aegean : Ierissos (1932) and Agios Efstratios (1968). J. Struct. Geol. 13, 205–214.
Pavlides, S., Tsapanos, T., Zouros, N., Sboras, S., Koravos, G., Chatzipetros, A., 2009. Using active fault data for assessing seismic hazard: a case study from NE Aegean sea, Greece. In: Earthquake Geotechnical Engineering Satellite Conference XVIIth International Conference on Soil Mechanics & Geotechnical Engineering, 2-3 October 2009, Egypt.
Pe-Piper, G., Piper, D.J.W., Koukouvelas, I., Dolansky, L.M., Kokkalas, S., 2009. Postorogenic shoshonitic rocks and their origin by melting underplated basalts: the miocene of Limnos, Greece. Bull. Geol. Soc. Am. 121, 39–54. https://doi.org/10.1130/B26317.1.
Peacock, D.C.P., Dimmen, V., Rotevatn, A., Sanderson, D.J., 2017. A broader classification of damage zones. J. Struct. Geol. 102, 179–192. https://doi.org/10.1016/j.jsg.2017.08.004.
Perri, F., Caracciolo, L., Cavalcante, F., Corrado, S., Critelli, S., Muto, F., Dominici, R., 2016. Sedimentary and thermal evolution of the Eocene-Oligocene mudrocks from the southwestern Thrace Basin (NE Greece). Basin Res. 28, 319–339. https://doi.org/10.1111/bre.12112.
Perrin, C., Manighetti, I., Gaudemer, Y., 2016. Off-fault tip splay networks: a genetic and generic property of faults indicative of their long-term propagation. Compt. Rendus Geosci. 348, 52–60. https://doi.org/10.1016/j.crte.2015.05.002.
Person, M., Hofstra, A., Sweetkind, D., Stone, W., Cohen, D., Gable, C.W., Banerjee, A., 2012. Analytical and numerical models of hydrothermal fluid flow at fault intersections. Geofluids 12, 312–326. https://doi.org/10.1111/gfl.12002.
Quevedo, R., de Andrade, T.J., Santos, L., Carvalho, B.R., Roehl, D., 2023. Assessment of fault damage zones in carbonate rocks based on numerical and sensitivity analyses. Tectonophysics 864, 230023. https://doi.org/10.1016/j.tecto.2023.230023.
Riley, P.R., Goodwin, L.B., Lewis, C.J., 2010. Controls on fault damage zone width, structure, and symmetry in the Bandelier Tuff, New Mexico. J. Struct. Geol. 32, 766–780. https://doi.org/10.1016/j.jsg.2010.05.005.
Rinaldi, A.P., Jeanne, P., Rutqvist, J., Cappa, F., Guglielmi, Y., 2014. Effects of fault-zone architecture on earthquake magnitude and gas leakage related to CO2 injection in a multi-layered sedimentary system. Greenhouse Gases: Sci. Technol. 4, 99–120. https://doi.org/10.1002/ghg.1403.
Rohmer, J., Allanic, C., Bourgine, B., Sulem, J., Suhett-Helmer, G., Ghabezloo, S., Pouya, A., Renard, F., Beucher, H., Mehl, C., Siavelis, M., Tardieu, N., 2014. Improving our knowledge on the hydro-chemo-mechanical behaviour of fault zones in the context of CO2 geological storage. Energy Proc. 63, 3371–3378. https://doi.org/10.1016/j.egypro.2014.11.366.
Rotevatn, A., Bastesen, E., 2014. In: Spence, G.H., Redfern, J., Aguilera, R., Bevan, T.G., Cosgrove, J.W., Couples, G.D., Daniel, J.-M. (Eds.), Soc. Spec. Publ., 374, pp. 79–95. https://doi.org/10.1144/SP374.12.
Rotevatn, A., Fossen, H., Hesthammer, J., Aas, T.E., Howell, J.A., 2007. In: Lonergan, L., Jolly, R.J.H., Rawnsley, K., Sanderson, D.J. (Eds.), Fractured Reservoirs.Geological, 270. Society Special Publication, pp. 55–71. https://doi.org/10.1144/GSL.SP.2007.270.01.04.

Rotevatn, A., Jackson, C.A.L., Tvedt, A.B.M., Bell, R.E., Blækkan, I., 2018. How do normal faults grow? J. Struct. Geol. 125, 174–184. https://doi.org/10.1016/j.jsg.2018.08.005.

Roure, F., Swennen, R., Schneider, F., Faure, J.L., Ferket, H., Guilhaumou, N., Osadetz, K., Robion, P., Vandeginste, V., 2005. Incidence and importance of tectonics and natural fluid migration on reservoir evolution in foreland fold-and-thrust belts. Oil Gas Sci. Technol. 60, 67–106. https://doi.org/10.2516/ogst:2005006.

Salvini, F., 2019. Daisy3, the structural data integrated system analyzer. Software version 5.38. Retrieved from. https://host.uniroma3.it/progetti/fralab/Downloads/Daisy_Program/.

Sanderson, D.J., Nixon, C.W., 2018. Topology, connectivity and percolation in fracture networks. J. Struct. Geol. 115, 167–177. https://doi.org/10.1016/j.jsg.2018.07.011.

Sanderson, D.J., Nixon, C.W., 2015. The use of topology in fracture network characterization. J. Struct. Geol. 72, 55–66. https://doi.org/10.1016/j.jsg.2015.01.005.

Sanderson, D.J., Peacock, D.C.P., Nixon, C.W., Rotevatn, A., 2019. Graph theory and the analysis of fracture networks. J. Struct. Geol. 125, 155–165. https://doi.org/10.1016/j.jsg.2018.04.011.

Savage, H.M., Brodsky, E.E., 2011. Collateral damage : evolution with displacement of fracture distribution and secondary fault strands in fault damage zones. J. Geophys. Res. 116, B03405 https://doi.org/10.1029/2010JB007665.

Shipton, Z.K., Cowie, P.A., 2003. A conceptual model for the origin of fault damage zone structures in high-porosity sandstone. J. Struct. Geol. 25, 333–344. https://doi.org/10.1016/S0191-8141(02)00037-8.

Shipton, Z.K., Cowie, P.A., 2001. Damage zone and slip-surface evolution over μm to km scales in high-porosity Navajo sandstone, Utah. J. Struct. Geol. 23, 1825–1844. https://doi.org/10.1016/S0191-8141(01)00035-9.

Siyako, M., Huvaz, O., 2007. Eocene stratigraphic evolution of the Thrace Basin, Turkey. Sediment. Geol. 198, 75–91. https://doi.org/10.1016/j.sedgeo.2006.11.008.

Smeraglia, L., Mercuri, M., Tavani, S., Pignalosa, A., Kettermann, M., Billi, A., Carminati, E., 2021. 3D Discrete Fracture Network (DFN) models of damage zone fluid corridors within a reservoir-scale normal fault in carbonates: multiscale approach using field data and UAV imagery. Mar. Petrol. Geol. 126, 104902 https://doi.org/10.1016/j.marpetgeo.2021.104902.

Soliva, R., Schultz, R.A., 2008. Distributed and localized faulting in extensional settings : insight from the North Ethiopian Rift – Afar transition area. Tectonics 27, 1-19. https://doi.org/10.1029/2007TC002148.

Storti, F., Balsamo, F., Cappanera, F., Tosi, G., 2011. Sub-seismic scale fracture pattern and in situ permeability data in the chalk atop of the Krempe salt ridge at Lägerdorf, NW Germany: inferences on synfolding stress field evolution and its impact on fracture connectivity. Mar. Petrol. Geol. 28, 1315–1332. https://doi.org/10.1016/j.marpetgeo.2011.03.014.

Storti, F., Billi, A., Salvini, F., 2003. Particle size distributions in natural carbonate fault rocks : insights for non-self-similar cataclasis. Earth Planet Sci. Lett. 206, 173–186. https://doi.org/10.1016/S0012-821X(02)01077-4.

Taymaz, T., Jackson, J., McKenzie, D., 1991. Active tectonics of the north and central Aegean Sea. Geophys. J. Int. 106, 433–490. https://doi.org/10.1111/j.1365-246X.1991.tb03906.x.

Taymaz, T., Yilmaz, Y., Dilek, Y., 2007. The geodynamics of the Aegean and Anatolia: introduction. In: Taymaz, T.Yilmaz, Y.Dilek, Y. (Eds.) .The Geodynamics of the Aegean and Anatolia. Geological Society Special Publication, 291, pp. 1–16. doi: 10.1144/SP291.1.

Torabi, A., Balsamo, F., Nogueira, F.C.C., Vasconcelos, D.L., Silva, A.C.E., Bezerra, F.H.R., Souza, J.A.B., 2021. Variation of thickness, internal structure and petrophysical properties in a deformation band fault zone in siliciclastic rocks. Mar. Petrol. Geol. 133, 105297 https://doi.org/10.1016/j.marpetgeo.2021.105297.

Torabi, A., Berg, S.S., 2011. Scaling of fault attributes: a review. Mar. Petrol. Geol. 28, 1444–1460. https://doi.org/10.1016/j.marpetgeo.2011.04.003.

Torabi, A., Ellingsen, T.S.S., Johannessen, M.U., Alaei, B., Rotevatn, A., Chiarella, D., 2020. Fault zone architecture and its scaling laws: where does the damage zone start and stop?. In: Ogilvie, S.R., Dee, S.J., Wilson, R.W., Bailey, W.R. (Eds.), Integrated Fault Seal Analysis.Geol. Soc. Spec. Publ., 496, pp. 99–124. https://doi.org/10.1144/SP496-2018-151.

Tranos, M.D., 2009. Faulting of Lemnos island; a mirror of faulting of the North Aegean Trough (northern Greece). Tectonophysics 467, 72–88. https://doi.org/10.1016/j.tecto.2008.12.018.

Vermilye, J.M., Scholz, C.H., 1999. Fault propagation and segmentation: insight from the microstructural examination of a small fault. J. Struct. Geol. 21, 1623–1636. https://doi.org/10.1016/S0191-8141(99)00093-0.

Wagner, H., Summers, S., 2005. Joints in faulting and folding. In: Mandl, G. (Ed.), Rock Joints: the Mechanical Genesis. Springer Berlin, Heidelberg, pp. 153–184.

Walsh, J.J., Watterson, J., 1988. Analysis of the relationship between displacements and dimensions of faults. J. Struct. Geol. 10, 239–247. https://doi.org/10.1016/0191-8141(88)90057-0.

Walter, B., Géraud, Y., Hautevelle, Y., Diraison, M., Raisson, F., 2019. Fluid circulations at structural intersections through the Toro-Bunyoro fault system (Albertine Rift, Uganda): a multidisciplinary study of a composite hydrogeological system. Geofluids 2019, 8161469. https://doi.org/10.1155/2019/8161469.

Wibberley, C.A.J., Yielding, G., Di Toro, G., 2008. In: Wibberley, C.A.J., Kurz, W., Imber, J., Holdsworth, R.E., Collettini, C. (Eds.), The Internal Structure of Fault Zones: Implications for Mechanical and Fluid-Flow Properties, 299. Geological Society Special Publication, pp. 5–33. https://doi.org/10.1144/SP299.2.